AD-A222 704

# REPORT DOCUMENTATION PAGE

Form Approved
OMB No. 0704-0188



| 1. AGENCY USE ONLY (Leave blank) | 2. REPORT DATE | 3. REPORT TYPE AND DATES COVERED |
|---|---|---|
| | April 24, 1990 | Final Report 4/1/88 - 3/31/90 |

**4. TITLE AND SUBTITLE**

Particle Simulation of Hypersonic Flow

**5. FUNDING NUMBERS**

AFOSR 88-0139

**6. AUTHOR(S)**

Donald Baganoff

AFOSR-TR- 90-0555

**7. PERFORMING ORGANIZATION NAME(S) AND ADDRESS(ES)**

Department of Aeronautics and Astronautics
Stanford University
Stanford, CA 94305

**8. PERFORMING ORGANIZATION REPORT NUMBER**

N/A

**9. SPONSORING/MONITORING AGENCY NAME(S) AND ADDRESS(ES)**

AIR FORCE OFFICE OF SCIENTIFIC RESEARCH
DIRECTORATE OF AEROSPACE SCIENCES
BOLLING AFB, DC 20332-6448

NA

**10. SPONSORING/MONITORING AGENCY REPORT NUMBER**

61102F
2307 A1

**11. SUPPLEMENTARY NOTES**

DTIC
ELECTE
MAY 25 1990
S D
D CB

**12a. DISTRIBUTION/AVAILABILITY STATEMENT**

APPROVED FOR PUBLIC RELEASE
DISTRIBUTION IS UNLIMITED

**12b. DISTRIBUTION CODE**

**13. ABSTRACT (Maximum 200 words)**

A limitation of the DSMC method is that it does not allow efficient use of vector architectures that are predominate in current supercomputers. A new selection rule for collisions between simulated molecules is developed which is highly compatible with vectorization. The collision-selection rule is shown to give identical results to the DSMC method in predicting shock-wave structure and in predicting the correct mean-free path variation with denisty and temperature for power-law interactions ranging from hard sphere to Maxwell molecule. Algorithmic improvements beyond those related to vectorization issues alone are also introduced, making possible simulations of single-species, rarefied, 3D hypersonic flows employing 10 million particles and 0.5 million cells. The performance of the algorithm on the Cray-2 ranges from 1 to 2 microseconds/particle/time-step. Roughly 500 to 1000 time-steps are needed to time average the results of a simulation, leading to run times of 2 to 5 hours on the Cray-2 for large problems.

Keywords:

"Original contains color plates: All DTIC reproductions will be in black and

**14. SUBJECT TERMS**

particle method, rarefied flow, direct simulation, Monte Carlo, collision selection

**15. NUMBER OF PAGES**

73

**16. PRICE CODE**

| 17. SECURITY CLASSIFICATION OF REPORT | 18. SECURITY CLASSIFICATION OF THIS PAGE | 19. SECURITY CLASSIFICATION OF ABSTRACT | 20. LIMITATION OF ABSTRACT |
|---|---|---|---|
| UNCLASSIFIED | UNCLASSIFIED | UNCLASSIFIED | |

NSN 7540-01-280-5500

Standard Form 298 (Rev. 2-89)

**Department of AERONAUTICS and ASTRONAUTICS**
**STANFORD UNIVERSITY**

Final Report

for the Period

April 1, 1988 to March 31, 1990

on

# PARTICLE SIMULATION OF HYPERSONIC FLOW

Grant No. AFOSR 88-0139

Submitted to the

Air Force Office of Scientific Research
Building 410, Bolling AFB, D. C. 20332
L. Sakell – Technical Officer

by the

Department of Aeronautics and Astronautics
Stanford University, Stanford, California 94305

Donald Baganoff – Principal Investigator

April 24, 1990

# INTRODUCTION

This final report is for work carried out under Grant No. AFOSR 88-0139 during the two year period from April 1, 1988 to March 31, 1990.

For vehicles that operate at altitudes above 80 km such as the Shuttle, the National Aerospace Plane, and the Aeroassist Flight Experiment, calculations based on the Navier-Stokes equations lead to erroneous results because of the very low densities. An alternative approach to the use of the Navier-Stokes equations, and one that is well suited to treating rarefied hypersonic flows, is to employ the Direct Simulation Monte Carlo (DSMC) method, a statistical procedure that simulates a gas flow by a large collection of particles. However, a limitation of the DSMC method is that it does not allow efficient use of vector architectures that are predominate in current supercomputers. Consequently, the computation speed is severely limited, thus restricting the problem size one can handle to principally one- and two-dimensional flows.

The size of a simulation may be measured in terms of the number of particles employed, and it is clear that more particles are needed for a 3D simulation than for a 1D or 2D simulation, if the same level of accuracy is to be obtained. Once the number of particles is set, the number of cells into which space is divided is also set, because the average number of particles per cell must be greater than a certain minimum value to reproduce the correct flow physics. Practical experience shows this lower limit to be about 15 particles per cell, assuming modest statistical accuracy. This number is far too small to give useful statistics in simulations of nonsteady flows, but for steady flows one may average the results over time, effectively increasing the sample size per cell to a level that gives acceptable statistics. To model a 3D problem, it would be desirable to have at least 500,000 cells (space of $128 \times 64 \times 64$ cells) at an average density of 20 particles per cell for a total of $10^7$ particles. If the gas consists of several species, then a still larger number would be required.

Basing an estimate on a single-species gas and using $10^3$ time steps for the required time averaging (20,000 samples per cell on average) we see that $10^{10}$ particle-time steps of computational effort is required to develop a solution. If the computation is to be carried out in a period of 3 hours, then a performance of roughly 1 microsecond

per particle per time step is required. Past experience has shown that this performance is about one to two orders of magnitude beyond the capability provided by the DSMC method implemented on the Cray family of computers. Recognizing that the ratio in computation time between a straightforward serial code and an efficiently vectorized code is roughly a factor of 15 to 20 on the Cray-2, it is clear that one must also consider other algorithmic improvements beyond those directly related to vectorization issues, if the necessary overall improvement in performance is to be attained.

Our work has focused on a reformulation of the DSMC method with the objective of designing a procedure that is optimized to the vector architecture found on the Cray-2. In this regard, we have developed a vectorizable collision-selection rule to replace the time-counter algorithm of the DSMC method so that vector processing can be more efficiently employed. This rule, which is used to statistically control the selection of both the type and number of colliding particle pairs, has been a key step in the development of the method. Additionally, our work has focused on finding a better balance between algorithmic complexity and the total number of particles employed in a simulation so that the overall performance of a particle simulation scheme could be greatly improved. Because of the rather significant algorithmic changes introduced, it was decided to first study a single-species, ideal gas, until full verification of the approach is achieved, prior to incorporating real gas effects.

## COMPLETED WORK

A major effort in the period was devoted to the writing of a paper [1], which was submitted for publication to the Physics of Fluids A. Because it outlines the main objective of our work and fully describes the approach we are taking, a copy of the manuscript is included in Appendix A. This work presents a detailed discussion of the development of our theory for a new selection rule governing collisions in a particle simulation of rarefied hypersonic flow. The new rule is particularly well suited for use on vector-oriented computers and it was specifically developed with the objective of taking advantage of the much higher computation speed that is available when running vectorized codes. In the paper we were able to show that shock-wave profiles predicted by our method agree exactly with the corresponding profiles

predicted by the Direct Simulation Monte Carlo (DSMC) method; and comparisons are presented there for both density and temperature, for hard sphere molecules and Maxwell molecules, and for shock-wave Mach numbers of 3 and 10.

In addition to the profile comparisons, the paper shows that the principal equation on which our theory is based can be related to the time-counter procedure used in the DSMC method. This gives further proof that the two methods are entirely equivalent. On the other hand, the selection rule governing collisions in our theory leads to an algorithm that can be efficiently implemented on a vector-oriented computer, while the time-counter method leads to a very inefficient implementation. A demonstration of the greater computational efficiency that can be realized on the Cray-2 supercomputer with our method is given by three examples in the paper. The three cases selected were all carried out as three-dimensional simulations, where the number of particles used ranged from $10^6$ to $10^7$ and the number of cells used ranged from $3 \times 10^4$ to $4 \times 10^5$.

A second major effort was the completion of a Ph. D. thesis by J. D. McDonald [2]. His thesis describes all of the work that was done to develop the theory we are using and to create the vectorized code for running on the Cray-2. His study, in effect, completes our work on the use of a single-species gas. Beyond the material presented in Ref. [1], his thesis gives a detailed account of the extension of the theory we are using to the case of a multiple species gas, introduces an arbitrary power law for molecular interactions, describes the approach he has developed to treat the rotational degrees of freedom for a diatomic molecule, introduces his proposed method for handling vibrational nonequilibrium, sets the stage for the inclusion of chemical nonequilibrium in our simulations, and gives the special programming steps taken to implement vectorized code on the Cray-2, as well as the additional programming steps taken to speed up many operations in general.

For example, he makes extensive use of lookup tables, as opposed to recalculating frequently used quantities. A special thermalized reservoir corresponding to the freestream state is used to supply particles for input into the freestream, as opposed to the use of random numbers and extensive calculations to generate this state. This same reservoir of thermalized particles is used as a source of samples for determining

the division of energy between vibration, rotation, and translation for colliding particles, as opposed to employing the Borgnakke-Larsen method with its heavy use of exponential functions. In addition, rather complete information on the programming used is presented along with a number of examples of the computed results for different simulated conditions. His thesis represents the basis on which all of our further investigations will be carried out. Also, his work has established the approach we will be using to carry out the vectorization of the work remaining to be done.

Different aspects of the above work were also reported in two AIAA papers which were given at the $24^{th}$ Thermophysics Conference at Buffalo in June, 1989. A paper by Woronowicz and McDonald [3] compares the simulated flow past a wedge with results from a corresponding experiment. Although the maximum Reynolds number that could be achieved in the simulation (for a reasonable computation time) was below the value reported for the experiment (3,560 versus 13,500), density, temperature, and pressure distributions were shown to compare very well, while the velocity profiles in the boundary layer were found to be similar but thicker due to the smaller Reynolds number.

The paper by Feiereisen and McDonald [4] is a product of the close collaboration between the work being done by our Stanford group and work by NASA-Ames scientists in the Aerothermodynamics Branch. In this case, Feiereisen (NASA-Ames) developed the programming for creating an arbitrary three-dimensional body on an IRIS Workstation, which then outputs to a file the resulting body geometry and associated constants needed for the boundary conditions. This file is then used in conjunction with McDonald's particle simulation program to obtain a solution for the rarefied hypersonic flow about the body. This collaborative effort led to the first successful attempt to study the full three-dimensional flow about the body shape representing the Aeroassist Flight Experiment (AFE).

Shown in Figs. 1 and 2 are the resulting solutions for the pressure and temperature distributions in the plane of symmetry and in a downstream wake cross-section of the AFE. The blunt body shape was simulated accurately by the front surface, but it was terminated by a flat plane on the aft side. The stair-stepped outline seen is a result of the use of a graphical polygon-fill routine to create the front surface,

but the terminating line was not defined. These runs were performed with $9.5 \times 10^6$ particles in a space of $120 \times 60 \times 60$ cells for a total of $4 \times 10^5$ mesh cells. The body diameter was 44 cell lengths, the upstream mean-free path length was 1.0 cells, and the Mach number was 35. Based on the body diameter, the Reynolds number was 2,300. Good statistics were obtained with time averaging over 800 time steps using a total of 4.5 hrs. of Cray- 2 single processor CPU time. Because of the large data sets required, these simulations made use of about 125 MW of Cray-2 central memory.

## MULTIPLE SPECIES

All of the work reported above was carried out for the case of a single-species gas. The stage was reached recently where we were confident that our approach had been adequately tested and that it is basically correct. Following this, considerable work was devoted to the creation of new code for handling multiple species. This code was written in the *C* programming language by Jeffrey McDonald, and time-critical elements of the code were being considered for translation into assembly language for the Cray-2, just as was done for the single-species code that we have been using. The *C* version of this code was created and tested before McDonald finished his thesis and he was able to give a full discussion of his efforts there. Some of his tests involved the computation of the shock-wave profile for a mixture of two hard-sphere, monatomic gases; and one of his test results is shown in Fig. 3, where a comparison is made between his predictions and results obtained using the DSMC method. As can be seen, the two agree very nicely and McDonald was able to conclude that his vectorized approach was working properly. Although McDonald finished his work as a student, he still participates in our research efforts as he now has a position at NASA-Ames, where he is associated with the Numerical Aeronautical Simulation (NAS) Program, and has been given responsibility for work that is closely connected to his previous work as a student.

At the start of calendar year 1990, several changes were made at the NAS computation facility at NASA-Ames, which we use to carry out our simulations. The change that has become most exciting to us was an upgrade in the version of the *C* compiler available for use on the Cray-2 and the Cray YMP. Once McDonald and

Fallavollita started testing the new compiler and set their sights on continuing the development of McDonald's code for multiple species, which Fallavollita is taking on as his thesis topic, it became evident that the new $C$ compiler contains new features, and a new capability, which greatly reduces the amount of work we will have to do.

The new features now provide the capability in the $C$ programming language that earlier could only be accessed after McDonald created considerable assembly language code, unique to the Cray-2. In fact, essentially all of our previous assembly language code can now be replaced by direct programming in $C$, assuming appropriate attention is given to the use of proper code constructs. McDonald's tests have shown that the new compiler has all of the capabilities that we need and that it produces code that executes just as fast as his earlier assembly language code. This means that we can write the programming for multiple species, and for the inclusion of chemical nonequilibrium, in a much shorter time than would have been possible with the earlier version of the $C$ compiler. In addition, this code can now be run on either the Cray-2 or the Cray YMP. Although the NAS Cray YMP has 128 MW of central memory versus 256 MW for the NAS Cray-2, it is twice as fast and represents a capability which we are interested in using. This development represents a very significant step forward in the rate at which we will be able to reach our goal of creating vectorized code that includes chemical nonequilibrium. The first report that will result from this new capability is an AIAA paper [5] to be given by Feiereisen and McDonald at the $5^{th}$ Joint Thermophysics and Heat Transfer Conference in Seattle in June, 1990. This paper will discuss our progress made in dealing with multiple species and, hopefully, initial steps toward the inclusion of nonequilibrium effects.

## CHEMICAL NONEQUILIBRIUM

Concurrent with the development of the code for multiple species, Brian Haas has been researching the problem of extending our simulation method to include the treatment of chemically reacting flows, while retaining the advantages inherent in vectorization present in the current code. His primary concern has been to develop the theory so that good compatibility would be found between the needs of the algebra for modeling chemical relaxation and the unique needs of vectorization. In this regard he

and McDonald have worked very closely so that the desired features would be present in the method selected as a result of his study.

One area in which Haas has made very nice progress is in his treatment of rotational and vibrational nonequilibrium. Following McDonald's lead, he makes use of the known relation between continuous and a quantized two-degree-of-freedom systems to cause the rotational (continuous) and vibrational (quantized harmonic oscillator) states to reach a common temperature (equilibrium), by mixing their energies in a way consistent with the fundamental physical assumption of statistical mechanics. This assumption holds that two states having the same energy with no degeneracies are equally probable. The primary purpose in using this approach is that the mixing of energies can be done using mathematics that does not involve extensive use of exponentials and transcendental functions, as is the case with the Borgnakke-Larsen method — the approach most frequently used in Bird's Direct Simulation Monte Carlo method. This is very important in minimizing the computation time that is taken in carrying out a simulation.

Some of the basic problems he has addressed have related to the question of how to treat recombination, which has not been adequately treated, and even ignored, in work by others. They have assumed that recombination would play a minor role in hypersonic blunt-body flows and dissociation would be the dominate feature. The principal reason for this assumption is that the theory for recombination, at the molecular level, has not been fully worked out. The difficulty one encounters is that recombination is basically a three-body process and a three-body collision is very difficult to handle in a particle method, where extremely rapid computation is essential. Also, there is no clear physics associated with the way one should distribute the total energy of the system under recombination in a way that meets all the requirements associated with matching the temperature dependence of the recombination rate coefficient, reproducing the correct equilibrium distribution for the different species, and establishing a common temperature among all the species of the mixture.

In Haas' work he has made careful use of detailed balance, which is a very important theoretical concept in both equilibrium and nonequilibrium thermodynamics. In addition, he has made good use of a very reasonable assumption that the total energy

of the system in recombination can be distributed among the component energies by increasing each of them in proportion to the energies they had before recombination. This method is exact for an equilibrium gas, but is not fully correct for a gas that is wholly out of equilibrium. However, because many other thermalizing processes are taking place at a much faster rate than recombination, and the fact that the fraction that undergoes recombination is very small, the resulting approximation is a very good one, and he has shown that it works extremely well.

Besides the presentation in his thesis which is expected to be finished in calendar year 1990, he is in the process of writing several papers on his work. The first of these will be an AIAA paper [6] to be given at the 5$\hat{\text{t}}$h Joint Thermophysics and Heat Transfer Conference in Seattle in June, 1990. He has been working diligently on it and the most recent draft of his paper is presented in Appendix B. Here, we can refer to his figures 4 through 8 to see how well his model works and to assess the state of his accomplishments. Figure 8 shows that he is able to fully handle a 5-species representation of air at temperatures that correspond to re-entry conditions.

## FLAT PLATE BOUNDARY LAYER

Michael Woronowicz has been studying the drag and heat transfer for a flat plate boundary layer by researching the literature and by carrying out simulations with our single-species code. The purpose of his work is to provide our group with the knowledge and experience needed so that we will be able to treat and handle the more complex boundary layers encountered in three-dimensional flows about the AFE body. It is our view that we must show that we are able to predict the simple case of a flat-plate boundary layer quite well, before we attack the more complex case of interest in our work.

He has taken two very important steps which place our group in a strong position to continue along our present path. First, he has devised a new way to correlate all of the existing experimental data so that the data collapse onto a single curve, instead of appearing as a family of curves with a free parameter; and second, he has

conducted numerous simulations with our code to compare results with these experimental data, which show that we are able to make predictions that compare with experimental results very well.

Figure 4 is taken from a paper that Woronowicz has been writing. It compares all of the available experimental data on flat-plate drag for the case of an adiabatic plate and for three different correlation methods: a) use of the viscous interaction parameter; b) the so-called slip parameter; and c) the new parameter introduced by Woronowicz. It is very clear that the new parameter is quite superior to the other two in correlating the experimental data. Woronowicz is able to show that this parameter works equally well for the case of a highly cooled plate, as well as for the case of heat transfer to a cold flat plate.

In Figs. 5 and 6 we show comparisons between his simulated results and the results of experiment, for the case of a cold flat plate and the case of an adiabatic, or hot, flat plate. His new correlation parameter is used in these two plots and it is clear that it is working extremely well. At present, more runs have been conducted for the case of the cold wall, and therefore, Fig. 5 appears more complete than Fig. 6. The figures show that the simulations are giving very good results over a wide range of conditions and that they blend in nicely with the data in the near-continuum regime.

Because of the large number of particles that can be used in our simulations, we are able to obtain nice resolution and striking pictures of the simulated flows. A typical example is shown in Fig. 7 where the Mach number distribution in the flow near the flat plate is displayed. It is of great interest to observe the velocity slip that occurs near the leading edge of the plate. This is strictly a macroscopic phenomena that occurs in a rarefied flow, as the boundary condition used for the individual reflected particles gives these particles random thermal components of velocity, at the plate temperature, but no mean motion.

## EFFECT OF SCALE

An important effect that has not been studied is the connection between computation time and the size of a simulation. One of the most useful properties of a

particle code which is based on statistical sampling is that the computational cost is proportional to the number of particles and the number of steps; that is, the same computational cost is incurred when doubling the number of particles as when the number of time steps is doubled. However, if doubling the number of particles leads to a better physical representation of a gas flow than doubling the duration of the averaging, then it is clear which arrangement one would choose, provided sufficient computer memory is available.

If one assumes that the theory for statistically independent random variables applies to a particle simulation, then one concludes that the fractional error, $\epsilon$, associated with a macroscopic variable, depends only on the size of the statistical sample. Therefore, it is given by $\epsilon = 1/\sqrt{NT}$, where $N$ is the number of particles in a cell and $T$ is the number of times steps used in time averaging. Because computation cost depends directly on the product $NT$, one concludes that the fractional error remains fixed, if cost is held fixed, independent of the size of the simulation, $N$. On this basis, it is obvious that one would choose to use a longer time average because it would tie up less of the computer resources. On the other hand, the situation may be quite different if statistical independence does not fully apply.

Figure 8 shows the results of a very preliminary test using our single-species code developed for the Cray-2. The test problem studied was the blunt-body flow produced by a two-dimensional flat plate in a Mach 8 flow of an ideal, diatomic, hard-sphere gas, where the Knudsen number, based on the plate width, was 0.1 and the plate temperature was held constant at the freestream value. The error was computed as the mean *rms* error of the pressure in a cell divided by the stagnation point pressure. Fortunately, the absolute error can be determined simply from a series of comparisons of the relative errors between the different runs, without having to know the exact solution. The curve shown is for a constant value of $NT$; and we see that the fractional error decreases dramatically as the number of particles in the simulation is increased, even though the total computation cost is held fixed. The figure indicates that the nonlinear physics present in the simulation requires that, in order to reach a level of error of 0.1 percent, it is better to employ a simulation having an average density of 100 particles per cell than to use 10 particles per cell together with a longer time average. In fact, the preliminary data indicate that, for a given

level of error, a certain minimum number density is needed, regardless of the duration of the time average used. This clearly helps to explain how to minimize computation cost in a particle simulation. This work has been carried out by Michael Fallovollita and the results of a more complete study are to be published soon.

## CONTINUING WORK

Over the past four years, we have enjoyed a very close working relationship with the Aerothermodynamics Branch at NASA-Ames Research Center, in particular with Dr. G. S. Deiwert (Branch Chief) and Dr. W. J. Feiereisen (Assistant Branch Chief), and have received support from their branch in a number of ways: grant funds to support students, use of their workstations and facilities by our students, collaborative effort between individuals in the Stanford and Ames groups, and access to the computation facilities available through the Numerical Aerodynamic Simulation (NAS) Program at Ames. At the present time our Stanford group consists of four Ph.D. students, and three scientists from NASA-Ames regularly attend our weekly research meetings (Feiereisen, McDonald and Boyd).

The collaborative effort between our respective groups was specifically planned to consist of an arrangement where our students would focus principally on theoretical questions and on computations that exercise and test new ideas, while the Ames effort would give greater focus to the solution of practical problems, employing the new computational capability developed. The main thrust of our continuing research is to push forward on the following four fronts:

1) to include chemical kinetics in our simulations so that thermochemical nonequilibrium among several different species may be handled;

2) to further develop our graphics display capability, along with suitable data analysis, to handle the huge data sets we encounter in our simulations;

3) to study rarefied hypersonic boundary layers on flat plates to guide our understanding of boundary layers on complex three-dimensional bodies; and

4) to apply these capabilities to the solution of practical problems of rarefied, real-gas, hypersonic, three-dimensional flows about aerodynamic bodies such as the AFE.

As the different efforts described above converge to a single working code, we will turn our attention to the solution of several practical problems involving real vehicles and real-gas flows. Here, our close collaboration with the NASA-Ames Aerothermodynamics group will be extremely useful, as the work will require the specification of reaction rates for different species, the use of realistic body geometries, questions of physical processes associated with gas-surface interactions, conditions of heat transfer at the body surface, and the altitude-Mach number flight envelope. One of the body geometries we plan to investigate thoroughly is the AFE body. These will consist of fully three-dimensional simulations employing over $10^7$ particles, $0.5 \times 10^6$ cells, and multiple species. The anticipated results ought to be very exciting and we are looking forward to the point in our work where we will be in a position to study data from such runs.

## REFERENCES


[1] D. Baganoff and J. D. McDonald, "A Collision-Selection Rule for a Particle Simulation Method Suited to Vector Computers," **Phys. Fluids**, July, 1990.

[2] J. D. McDonald, "A Computationally Efficient Particle Simulation Method Suited to Vector Computer Architectures," Ph.D. thesis, Stanford University, December, 1989. Also, published as a report by the Department of Aeronautics and Astronautics, SUDAAR Report No. 589.

[3] M. Woronowicz and J. D. McDonald, "Application of a Vectorized Particle Simulation in High-Speed Near-Continuum Flow," AIAA Paper No. 89-1665, $24^{th}$ Thermophysics Conference, Buffalo, June 12-14, 1989.

[4] W. Feiereisen and J. D. McDonald, "Three-Dimensional Discrete Particle Simulation of an AOTV," AIAA Paper No. 89-1711, $24^{th}$ Thermophysics Conference, Buffalo, June 12-14, 1989.

[5] W. Feiereisen and J. D. McDonald, "Improved Three-Dimensional Discrete Particle Simulation about the AFE Geometry," AIAA Paper No. 90-1778, $5^{th}$ Joint Thermophysics and Heat Transfer Conference, Seattle, June 18-20, 1990.

[6] B. Haas, "Fundamentals of Chemistry Modeling Applicable to a Vectorized Particle Simulation," AIAA Paper No. 90-1749, $5^{th}$ Joint Thermophysics and Heat Transfer Conference, Seattle, June 18-20, 1990.

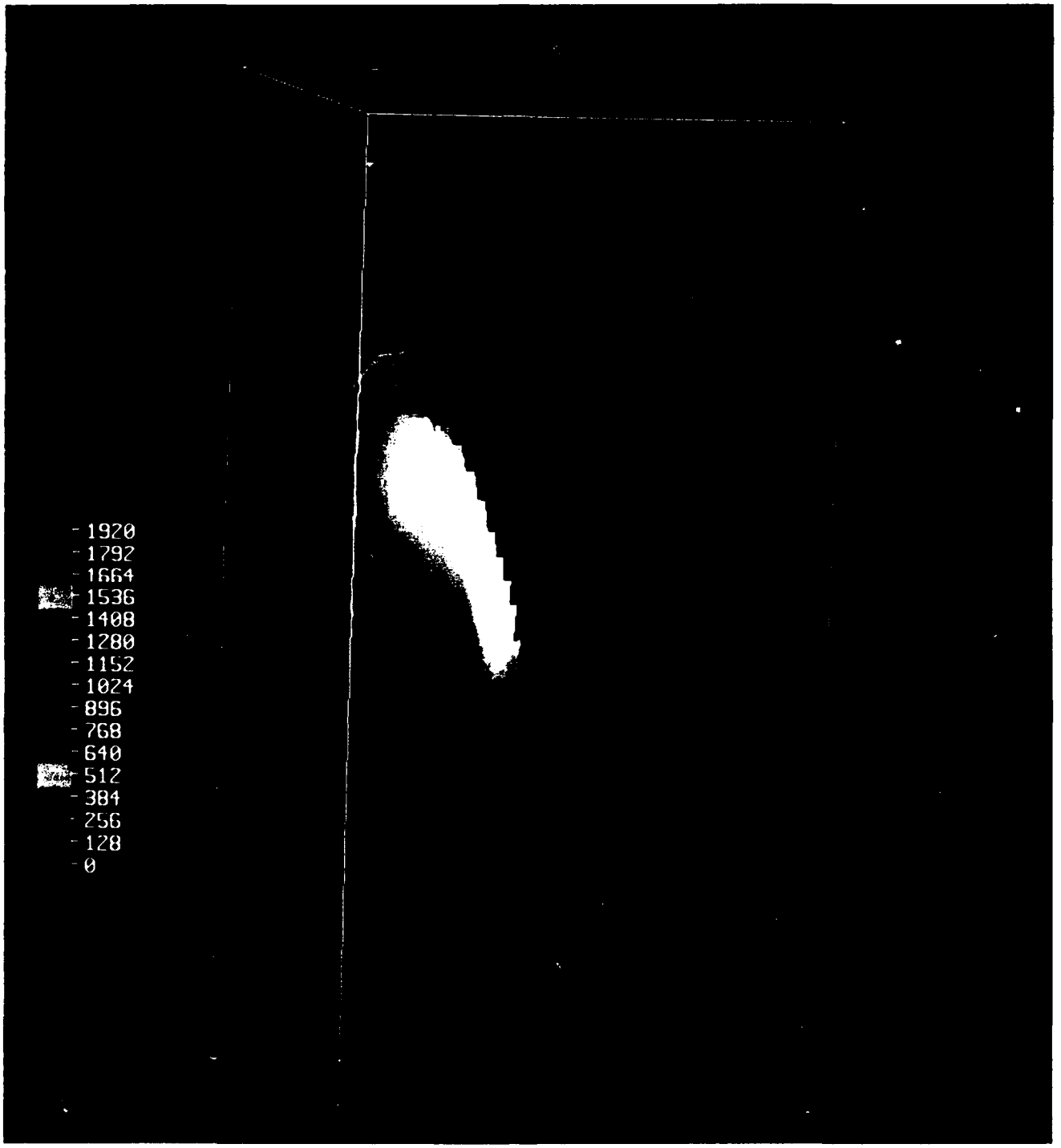


Fig. 1. Pressure distribution in the central plane of the AFE body and in a downstream wake cross-section of the flow. The simulation models the AFE body at an altitude of 90 km and a Mach number of 35. The gas is nitrogen, treated as ideal.

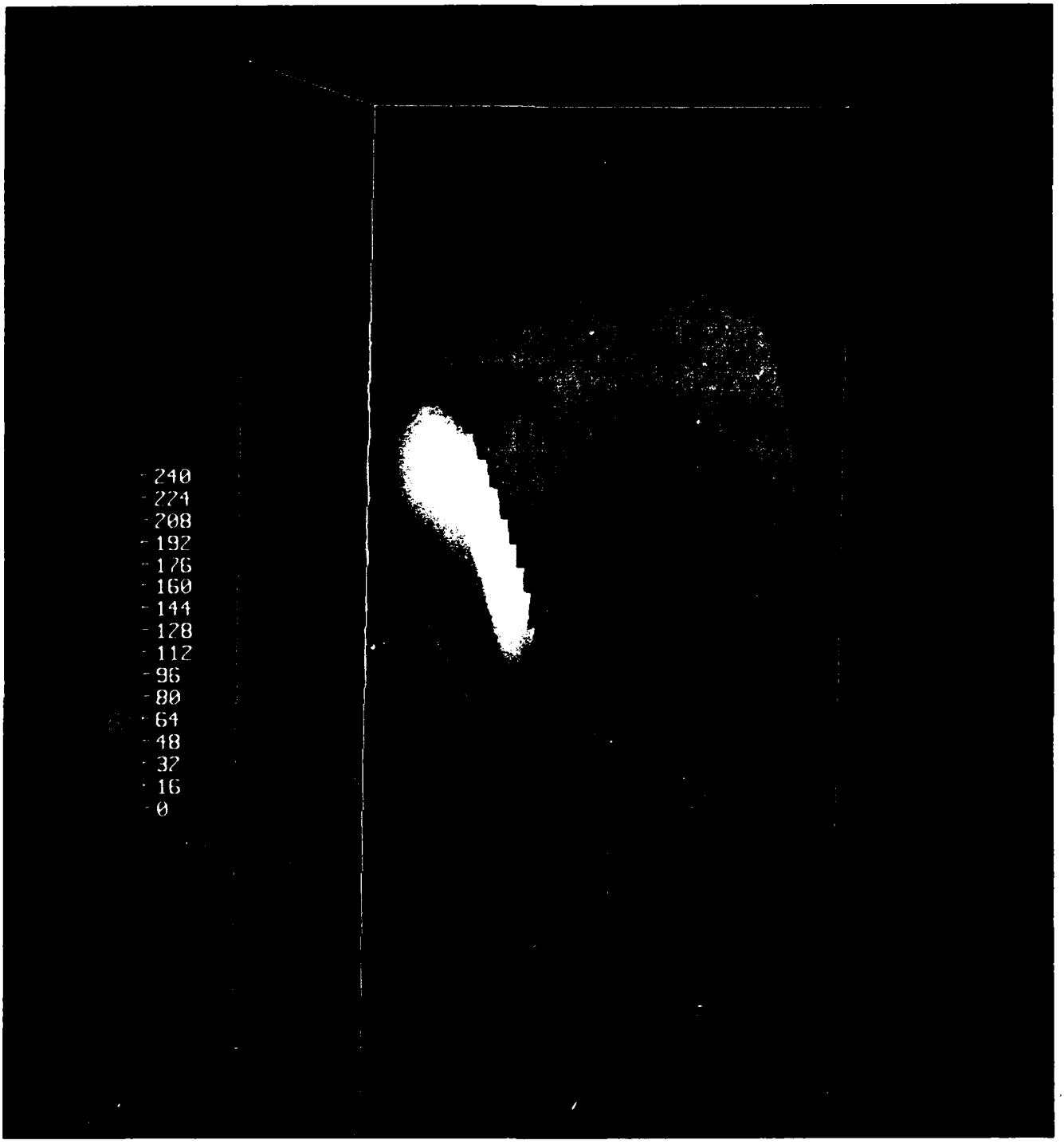


Fig. 2. Temperature distribution in the central plane of the AFE body and in a downstream wake cross-section of the flow. The simulation models the AFE body at an altitude of 90 km and a Mach number of 35. The gas is nitrogen, treated as ideal.

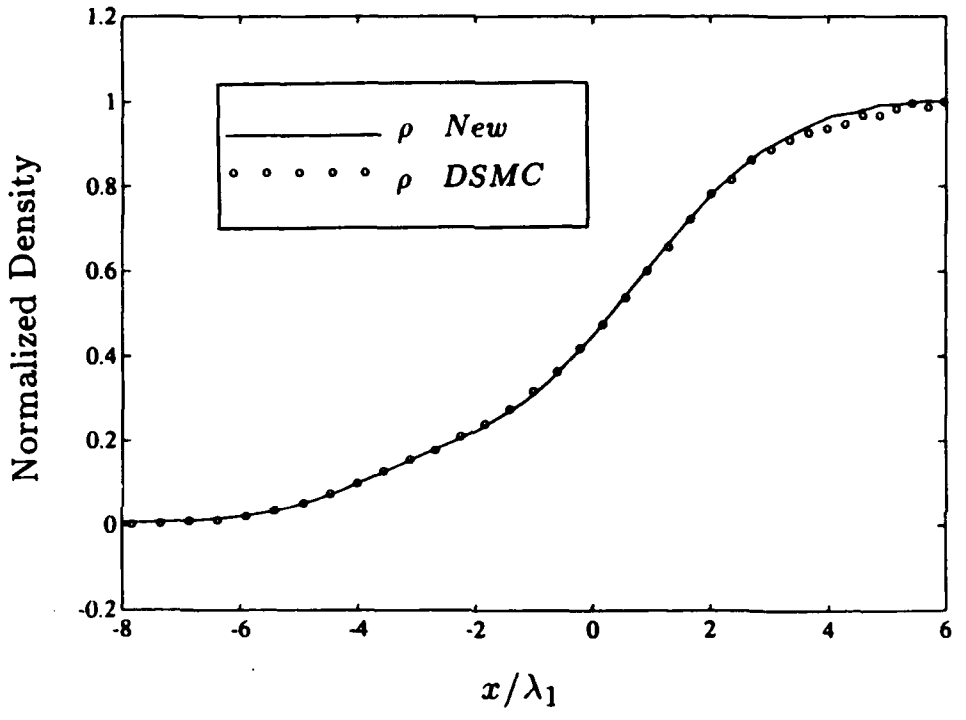


Fig. 3. Density distribution in a shock wave for a hard-sphere, monatomic, binary mixture of gases and a Mach number of 10. The heavy species is 15 times as massive as the light species and is present in a concentration of 0.20 of that of the light species.

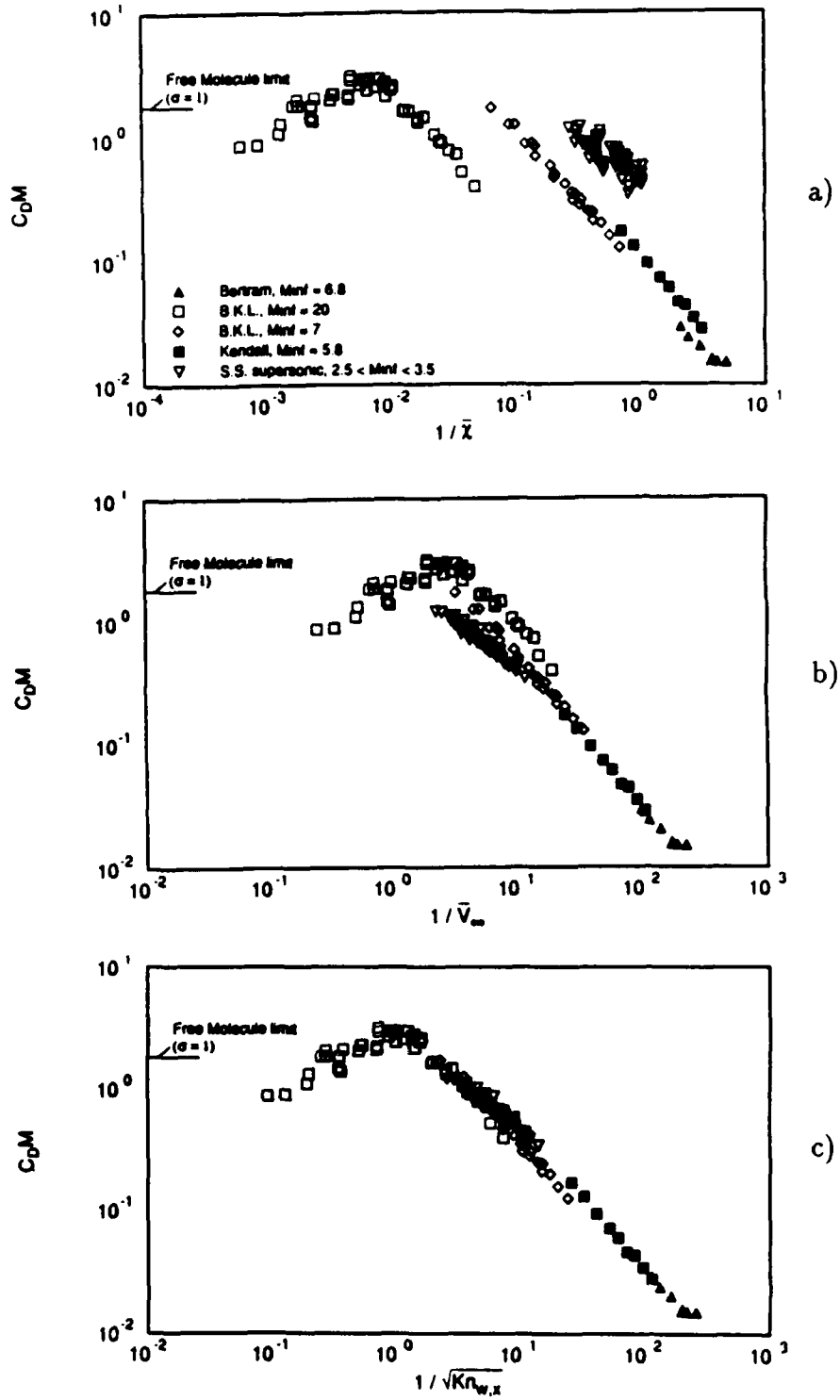


Fig. 4. Drag coefficient for a flat plate for three different hypersonic correlation parameters: a) use of the viscous interaction parameter; b) the so-called slip parameter; and c) the new parameter introduced by Woronowicz.

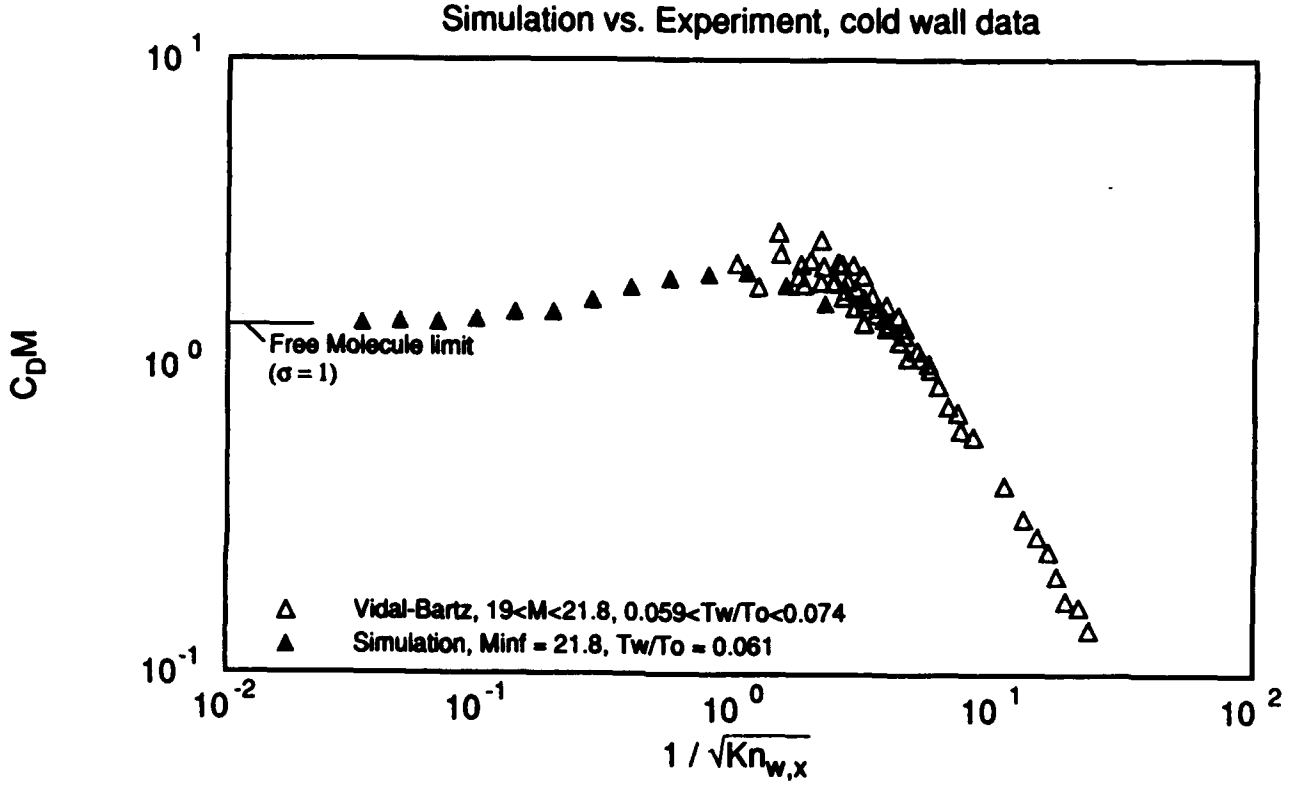


Fig. 5. Comparison of simulated results versus experiment for the drag coefficient on a cold flat plate. Simulations designated by the solid symbol.

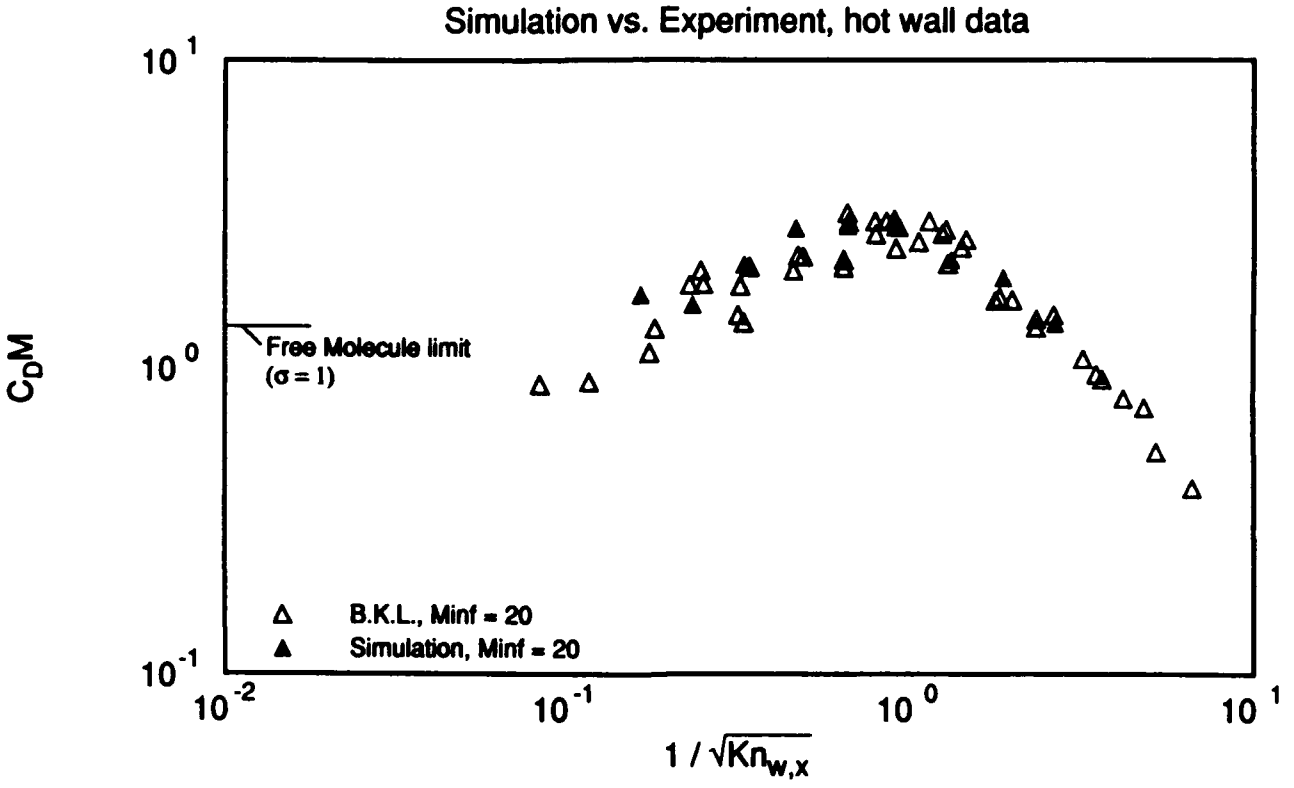


Fig. 6. Comparison of simulated results versus experiment for the drag coefficient on an adiabatic flat plate. Simulations designated by the solid symbol.

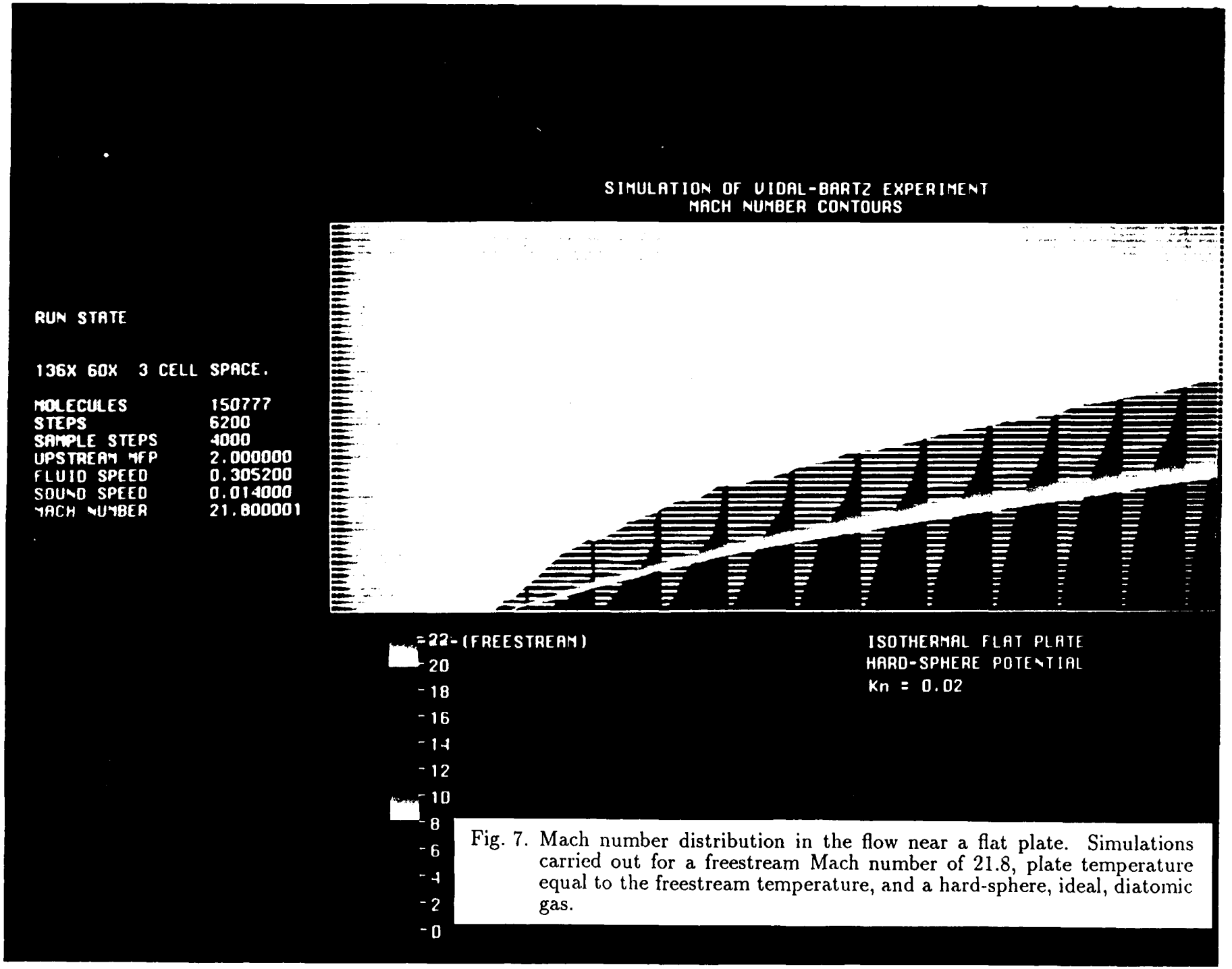


Fig. 7. Mach number distribution in the flow near a flat plate. Simulations carried out for a freestream Mach number of 21.8, plate temperature equal to the freestream temperature, and a hard-sphere, ideal, diatomic gas.

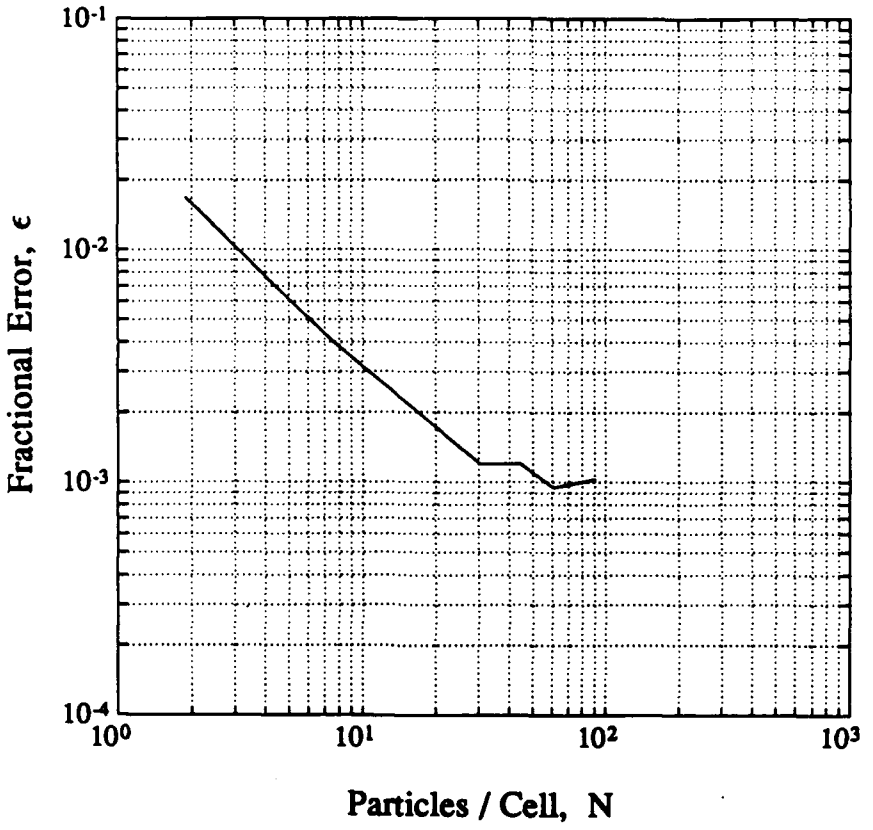


Fig. 8. Fractional error, $\epsilon$, for the pressure variable, versus the average number of particles per cell, $N$, for a fixed compuational effort. Curve shown is for the computational cost $NT = 2\times10^5$.

# APPENDIX A

# A collision-selection rule for a particle simulation method suited to vector computers

D. Baganoff and J. D. McDonald
Department of Aeronautics and Astronautics
Stanford University, Stanford, CA 94305

Abstract

A theory is developed for a selection rule governing collisions in a particle simulation of rarefied gas-dynamic flows. The selection rule leads to an algorithmic form that is highly compatible with fine grain parallel decomposition, allowing for very efficient utilization of supercomputers having vector or massively parallel SIMD architectures (single instruction multiple data). A comparison of shock-wave profiles obtained using both the selection rule and Bird's Direct Simulation Monte Carlo (DSMC) method show excellent agreement. This serves to establish the validity of the method, as the DSMC method is known to compare well with experimentally determined shock-wave profiles. In addition, the equation on which the selection rule is based is shown to be directly related to the time-counter procedure in the DSMC method, further establishing their equivalence. The results of several example simulations of representative rarefied flows are presented, for which the number of particles used ranged from $10^6$ to $10^7$, demonstrating the greatly improved computational efficiency of the method.

PACS numbers:

47.45.-n

51.10.+y

47.10.+g

47.40.Ki

# I. INTRODUCTION

The most widely used particle method for simulating a rarefied gas-dynamic flow is the Direct Simulation Monte Carlo (DSMC) method.[1,2] This method was introduced by G. A. Bird in the 1960s and has been advanced to the state where it is reliable, quite accurate and can handle rather general conditions of gas complexity and flow geometry. The main problem that arises in applying the method is that the principal algorithm employed contains logic which leads to conditional branching of a type that does not allow one to make effective use of supercomputers having a vector architecture, such as the Cray-2, or a massively parallel SIMD architecture (single instruction multiple data) such as the Connection Machine.

Because the execution speed of an efficiently vectorized code is over an order of magnitude faster on a vector oriented machine such as the Cray-2 than the speed of the same code when limited to scalar execution, it is important to explore methods that fully utilize these features. In addition, many of the projections estimating future increase in computational capability are principally based on extensive use of parallelism, requiring scientific applications to be properly structured to use such architectures effectively.

It is well known that Monte Carlo schemes in general do not vectorize well, as this problem has been addressed a number of times, particularly in the area of plasma physics. In a recent fluid mechanical study, Ploss vectorized a modified Nanbu algorithm, a simulation method for solving the Boltzmann equation, and concluded that the predominantly scalar Bird scheme was still the faster approach.[3] However, in light of the fact that over an order of magnitude decrease in computation time could be realized if the DSMC approach could be restructured to operate in a vector fashion, there is a strong motivation to seek ways to reformulate the algorithms utilized in the DSMC method which are presently limited to scalar execution.

To identify the elements that slow computation in the DSMC method and to understand the kind of changes required, we first outline the general steps that characterize a particle method and then focus the discussion on the particular step which represents Bird's time-counter procedure and the problems associated with its use. This is followed by the development of a theory, leading to an algorithmic structure for a selection rule governing collisions that is highly compatible with fine grain parallel decomposition. A comparison of shock-wave profiles obtained using both the selection rule and Bird's DSMC method show

excellent agreement. This serves to establish the validity of the selection rule, as the DSMC method is known to compare well with experimentally determined shock-wave profiles. In addition, the equation on which the selection rule is based is shown to be directly related to the time-counter procedure in the DSMC method, further establishing their equivalence. Finally, the results of several example simulations are presented, where large numbers of particles are used in the simulations, to demonstrate the greatly improved computational efficiency of the present method.

## II. STEPS IN A PARTICLE METHOD

In outlining the steps taken in a particle method, it is most convenient to consider a region of space free of boundaries or other special consideration. Also, we assume the entire space has been conceptually divided into a suitable arrangement of cells, similar to the approach taken in a finite element method. The overall procedure in a particle simulation, which applies at each time step $\Delta t$, can be represented by the following six steps.

(i) Advance all particles in space at constant velocity for the time $\Delta t$ and ignore possible collisions.

(ii) Use the new spatial positions and sort the particles into individual cells.

(iii) For a given cell in physical space, choose a pair of particles at random.

(iv) Use a selection rule to determine whether the pair formed is selected for collision. The selection rule also determines the total number of sample pairs formed for each cell and the distribution of colliding pairs over relative velocity. In order to simulate a real flow, these values must be consistent with those predicted by kinetic theory.

(v) If accepted for collision, conserve momentum and energy while colliding the pair to find their new states. The orientation of the relative velocity vector after collision is chosen randomly in correspondence with the scattering properties of the intermolecular potential considered.

(vi) Return to step (iii) to process the proper number of pairs in each cell and then to process all cells.

The above listing is presented primarily for purposes of discussion, since some of the steps are often combined or altered in particular applications.

The sorting operation in step (ii) and the pair selection process in step (iv) prove to be the most troublesome in writing efficient code for a computer having a vector or massively parallel SIMD architecture. The time-counter procedure in Bird's DSMC method corresponds to step (iv). To describe it, we assume the particles have been sorted into individual cells, i.e., steps (i) through (iii) have been completed. The time-counter procedure consists of the following three operations.

(a) Retain the randomly chosen pair if $R < \sigma_T g/(\sigma_T g)_{\max}$.

(b) For each pair retained, compute $\tau = 2/(Nn\,\sigma_T g)$.

(c) Collide pairs while $\tau_1 + \tau_2 + \tau_3 + \ldots \leq t$ for their cell.

In step (a), $R$ represents a uniformly distributed random number in the range [0, 1], $g$ is the relative speed of the particle pair, $\sigma_T$ is the total collision cross-section, and *max* denotes the largest value for the cell. In step (b), $n$ is the number density and $N$ is the number of particles in a cell. In step (c), the subscripts represent all the pairs accepted for collision in a given cell, and $t$ is the current time measured from the start of the simulation.

As is immediately obvious, the procedure contains two conditional branching statements, one in (a) and one in (c). Step (c) proves to be more difficult to vectorize, because the point at which the calculation terminates is not known *a priori* and it may be widely different for different cells. In the application of the algorithm, one discovers when to terminate the calculation only during the calculation itself. This is the concept of data dependency and we will return to the problem it presents in our discussion below. With regard to the physics, it is clear that the branching logic is instrumental in determining the total sample size for each cell. It selects the fraction that is to be retained for collision and it selects the distribution of relative speeds over the chosen pairs (i.e., large values of $\sigma_T g$ generate small values of $\tau$, and consequently, more of these are needed to produce the required sum).

The well-known success of the DSMC method in being able to predict a variety of experimental conditions has been widely recognized as providing a strong argument in support of its use. Its theoretical justification is based on the argument that, when the above steps

are carried out a large number of times, for a large number of particles, they lead to the single-particle collision frequency given by

$$\Theta = n\overline{\sigma_T g}, \tag{1}$$

where the overbar represents a mean quantity in the sense discussed by Bird.[4] Following similar logic, our approach is to return to the basic relation from which the well-known bimolecular collision rate for an equilibrium gas is derived and develop a relation for the nonequilibrium state that leads to a selection rule governing collisions that does not contain the data dependency represented by step (c).

## III. BIMOLECULAR COLLISION RATE

The bimolecular collision rate is usually derived for the case of an equilibrium gas and a hard-sphere molecule. This is because the velocity distribution function is known for the equilibrium state and the total collision cross-section for a hard-sphere molecule is clearly defined and finite, and the associated scattering is isotropic. As a consequence, the algebraic steps and required integrations can be carried out in a straightforward way. We will assume a hard-sphere molecule in our initial development, but the gas will not be assumed to be in equilibrium.

The numerical value of the (integrated) bimolecular collision rate gives the total number of pair collisions occurring between two species per unit of time in a unit volume. However, in order to handle rarefied flows, specific knowledge concerning the functional dependence of the pair collision rate on the relative velocity is needed for the case of a nonequilibrium gas. To obtain this information one must start with the basic expression for the collision rate between two species $A$ and $B$ given by[5]

$$\tilde{z}_{AB}\, d\boldsymbol{C}\, d\boldsymbol{Z} = \frac{n_A n_B}{1+\delta_{AB}} f_A(\boldsymbol{C}) f_B(\boldsymbol{Z}) (\pi d_{AB}^2)\, g\, d\boldsymbol{C}\, d\boldsymbol{Z}, \tag{2}$$

where $n_A$ is the number density, $f_A$ is the velocity distribution function, and $\boldsymbol{C}$ is the molecular velocity, all for specie $A$. Also, $d_{AB}$ is the average diameter for the two molecules and $g$ is their relative speed. For convenience, we use the notation $d\boldsymbol{C} = dC_x dC_y dC_z$. The Kronecker delta is used to account for the fact that $AB$ collisions are the same as $BA$ collisions when $A$ and $B$ are the same specie.

Equation (2) can be written in terms of the relative-velocity vector $(\boldsymbol{Z} - \boldsymbol{C})$ by use of the transformation

$$\boldsymbol{g} = \boldsymbol{Z} - \boldsymbol{C}$$

$$\boldsymbol{G} = (m_A \boldsymbol{C} + m_B \boldsymbol{Z})/(m_A + m_B),$$

where $\boldsymbol{g}$ is the relative-velocity vector for the colliding pair, and $\boldsymbol{G}$ is the center-of-mass velocity vector. For this case, the Jacobian of the transformation is unity, and therefore, we have $d\boldsymbol{C}\, d\boldsymbol{Z} = d\boldsymbol{G}\, d\boldsymbol{g}$. On introducing the transformation into (2) and integrating over $\boldsymbol{G}$, to obtain an expression in terms of $\boldsymbol{g}$ alone, one encounters the following integral operator

$$F(\boldsymbol{g}) = \int_{-\infty}^{\infty} f_A(\boldsymbol{G} - \frac{m^*}{m_A}\boldsymbol{g})\, f_B(\boldsymbol{G} + \frac{m^*}{m_B}\boldsymbol{g})\, d\boldsymbol{G}, \tag{3}$$

where $m^* = m_A m_B/(m_A + m_B)$ is the reduced mass. Therefore, Eq. (2) can be written

$$z_{AB}\, d\boldsymbol{g} = \frac{n_A n_B}{1 + \delta_{AB}} F(\boldsymbol{g}) d\boldsymbol{g} (\pi d_{AB}^2) g, \tag{4}$$

where a distinction between $\tilde{z}_{AB}$ and $z_{AB}$ is made to account for the different dimensions in the two equations. Equation (4), as it stands, has the proper form to develop our desired collision-selection rule, but it is useful to first review the fact that in many instances $F(\boldsymbol{g})$ has a very simple structure, which proves to greatly improve the utility of applying a statistical method to (4).

The function $F(\boldsymbol{g})$ describes how AB pairs are distributed as a function of their relative velocity vector $\boldsymbol{g}$, and clearly, it is a function of three independent variables. However, we will show that it is always a rather smooth function, and that it can often be approximated by a function of the relative speed g alone, i.e., a single independent variable. This is in contrast to the velocity distribution function $f(\boldsymbol{C})$, which has the potential for being a rather complex three-dimensional function. For example, it assumes a bimodal distribution in the upstream portion of a shock wave. The purpose of reviewing the simple structure of $F(\boldsymbol{g})$ is that, in using a statistical sampling scheme to evaluate Eq. (4), a far smaller number of samples can be used than would otherwise be necessary, and this clearly represents a very important practical consideration.

In establishing the fact that $F(\boldsymbol{g})$ is a smooth function, let's first consider the case of a single specie gas, for which the integral corresponding to (3) is given by

$$F(\boldsymbol{g}) = \int_{-\infty}^{\infty} f(\boldsymbol{G} - \boldsymbol{g}/2) f(\boldsymbol{G} + \boldsymbol{g}/2)\, d\boldsymbol{G}. \tag{5}$$

The first important observation we make concerning (5) is that it produces an even function of the relative velocity vector $\boldsymbol{g}$, i.e., we have

$$F(\boldsymbol{g}) = F(-\boldsymbol{g}). \tag{6}$$

We note that this is a general result and it does not depend on any assumptions whatsoever; it holds for any conceivable velocity distribution function, $f$.

The second observation is that the integral can be carried out exactly for the case of an equilibrium gas, and it leads to the expression

$$F^0(g) = \left(\frac{m}{4\pi kT}\right)^{3/2} \exp\left(-\frac{m}{4kT}g^2\right). \tag{7}$$

In this case $F^0(g)$ is a function of the scalar magnitude $g$ alone. That is, the function is not only symmetric but it is also spherically symmetric.

The third and final observation we make concerning the integral operator (5) is that it has the unexpected property of satisfying the central limit theorem. This can be seen as follows. For the case of a single independent variable, the convolution integral is defined by

$$f * f = \int_{-\infty}^{\infty} f(x-\xi)f(\xi)d\xi, \tag{8}$$

and a known result of the central limit theorem is represented by

$$f * f * f * f * \cdots \longrightarrow \text{gaussian}\ .$$

The corresponding operator suggested by (5) is different from (8) in the position of the minus sign, the appearance of the variable $x/2$, and in the presence of the argument $(\xi + x/2)$; therefore, we define a new operator by

$$f\#f = \int_{-\infty}^{\infty} f(\xi - x/2)f(\xi + x/2)d\xi. \tag{9}$$

We first note that the integrand in (8) could be replaced by $f(x/2-\xi)f(x/2+\xi)$ and the conclusions of the central limit theorem would still hold. This can be seen by a simple transformation of variables that leads back to Eq. (8). On using the operator defined by (9), we can now write

$$\begin{aligned} f\#f\#f\#f\#\cdots &= (f\#f)\#(f\#f)\#(f\#f)\#\cdots \\ &= e\#e\#e\#e\#\cdots \\ &= e * e * e * e * \cdots \longrightarrow \text{gaussian}\ , \end{aligned}$$

where $e$ is defined to be an even function; and where the second step makes use of (6), while the third step makes use of the fact that (8) and (9) are equivalent when $f$ is an even function.

At this point we have demonstrated that the operator defined by (5) satisfies the central limit theorem for the case of a single independent variable. However, it is easy to see that the results can be generalized in the following way. If one forms the Fourier transform of both sides of (9), makes use of the transformation $u = (\xi - x/2)$ and $v = (\xi + x/2)$ and notes the separation of variables, one obtains the relation $F(\omega) = f(-\omega)f(\omega)$, where $\omega$ is the transform variable. For the case of three independent variables, one introduces the three-dimensional transform variable $\boldsymbol{\omega}$ and performs exactly the same operation on (5), which again produces a product of Fourier transforms given by $f(-\boldsymbol{\omega})f(\boldsymbol{\omega})$. It is easy to see that repeated applications of the operator defined by (9), or (5), lead to repeated products of the same Fourier transforms. This is the property one uses in proving the central limit theorem, namely, one shows that the resulting expression, suitably normalized, tends toward the Fourier transform of the gaussian distribution.[6] The same principle can be used to show that Eq. (3) also has this property, however, its convergence to a gaussian is not as rapid because of the potential asymmetry present, i.e., one obtains $f_A(-\boldsymbol{\omega})f_B(\boldsymbol{\omega})$.

We now see that when the integral operator in (5), or (3), is applied a large number of times it produces the gaussian or Maxwellian distribution. The significance of this result is based on the fact that the central limit theorem is a very powerful theorem, in the sense that only a few applications are required to obtain a very close approximation to the gaussian distribution. The quick convergence to a gaussian distribution is best seen by considering several simple examples. If we assume a one-dimensional asymmetric function for $f$, as shown in Fig. 1(a), then a single application of the operator given by (9) leads to the symmetric function $F$ seen in Fig. 1(b). Here we see that the symmetric function $F$ is beginning to look like the gaussian distribution.

A second example, which makes use of a three-dimensional representation for $f$, is shown in Fig. 2. The integration required by (5) can be carried out analytically in three dimensions, if $f$ is assumed to be given by a spherically symmetric Cauchy distribution $(1/(\alpha + x^2))$. Normalization requires that the Cauchy distribution be truncated, because the required integral is otherwise divergent. The truncated Cauchy distribution used, and

the corresponding equilibrium distribution having the same total energy, are shown in Fig. 2(a). The result of the application of the operator (5) on both functions, shown in Fig. 2(b), makes it clear that the action of the central limit theorem is so strong that the two results for $F(\boldsymbol{g})$ are very nearly the same. For use in our discussion below, we also show in Fig. 2(c) the corresponding distribution functions for the relative speed (magnitude), which we define as $R(g)$.

The observations made above can now be used to introduce an excellent approximation for (5), which can then be used for a better understanding of the exact relation (4). Because of the properties of the central limit theorem, we know that $F(\boldsymbol{g})$ tends towards the gaussian distribution; and according to (6) it is guaranteed to be symmetric. We can therefore approximate (5) by a spherically symmetric function. However, this spherically symmetric function is not the equilibrium function (7) when the gas is out of translational equilibrium (see Fig. 2(c)). The approximation suggested is therefore the replacement of the symmetric function $F(\boldsymbol{g})$, which is a function of three independent variables, by a spherically symmetric function, $F(g)$, which is a function of only one independent variable. Using this approximation and noting that the differential element $d\boldsymbol{g}$ becomes $4\pi g^2\, dg$ for the case of spherical symmetry, the expression for the speed-dependent bimolecular collision rate for a single specie, hard-sphere gas is obtained from (4) and becomes

$$z_{AB}\, dg = \frac{n^2}{2}\left[4\pi g^2 F(g)\, dg\right](\pi d^2)\, g.$$

On introducing the following definition

$$R(g)\, dg = 4\pi g^2 F(g)\, dg, \tag{10}$$

and on introducing the time interval, $\Delta t$, our approximate relation becomes

$$z_{AB}\, dg\Delta t = \left\{\frac{n^2}{2} R(g)\, dg\right\}[(\pi d^2) g\Delta t]. \tag{11}$$

The partitioning shown in (11) and the inclusion of the time step $\Delta t$ are both introduced for convenience below. The exact form of (11) is of course Eq. (4), which we repeat using the same format employed in (11).

$$z_{AB}\, d\boldsymbol{g}\Delta t = \left\{\frac{n_A n_B}{1+\delta_{AB}} F(\boldsymbol{g}) d\boldsymbol{g}\right\}[(\pi d_{AB}^2) g\Delta t] \tag{12}$$

To emphasize the fact that (11) is exact as well for the equilibrium state, we can use it to derive the known bimolecular collision rate for a single specie hard-sphere gas in equilibrium. Defining $Z_{AB}$ to be the integrated bimolecular collision rate, and dropping the $\Delta t$ from (11), we have

$$Z_{AB} = \frac{n^2}{2}(\pi d^2) \int_0^\infty g\, R(g)\, dg.$$

For the equilibrium state, we use (7) and (10) to evaluate the integral, which yields the well-known result

$$Z_{AB} = \frac{n^2}{\sqrt{2}}(\pi d^2)\bar{C}, \tag{13}$$

where the mean molecular speed for an equilibrium gas, $\bar{C}$, is given by

$$\bar{C} = \sqrt{8kT/\pi m}\,. \tag{14}$$

Because Eq. (11) is conceptually simpler than the exact expression (12), we start with its discussion. The left-hand side of Eq. (11) represents the number of binary collisions that occur in a unit volume in the speed range $g$ to $g+dg$, in the time interval $\Delta t$. The right-hand side of the equation can be viewed several different ways, depending on how one chooses to group it. For large n, the quantity $n^2/2$ is approximately equal to the number of pairs that can be formed out of $n$ particles in a unit volume. The function $R(g)$ is the distribution of pairs over the relative speed $g$. Therefore, the quantity enclosed by braces is the number of pairs found in a unit volume in the speed range $g$ to $g + dg$. Now, the expression in square brackets is the volume swept out by the hard-sphere particle in the time $\Delta t$ as it moves at speed $g$. If this small volume is viewed in conjunction with the larger unit volume being considered, then its numerical value can be interpreted as the probability that the particle pair will be found in the small volume (this is the same basic concept used in setting up Eq. (2)). Using this interpretation, we can write Eq. (11) as follows

$$z_{AB}\, dg \Delta t = S\, R(g) dg\, P_s, \tag{15}$$

where $S$ is the sample size (for a unit volume) and $P_s$ is the probability of a binary collision. In this case we are using the two relations

$$S = n^2/2, \tag{16}$$

$$P_s = (\pi d^2) g \Delta t. \tag{17}$$

The statistical sampling scheme defined by Eq. (15) is to sample a unit volume $S$ times, saving only the pairs falling in a given speed range, and then save only the pairs for which a uniform random number in the range [0, 1] is less than the fraction $P_s$. The number of pairs retained is the number $z_{AB}\, dg\, \Delta t$.

Following the grouping used in (15), we can write the exact relation (12) in the same form and it leads to the expression given by

$$z_{AB}\, d\boldsymbol{g} \Delta t = S\, F(\boldsymbol{g}) d\boldsymbol{g}\, P_s, \tag{18}$$

where in this case, we have

$$S = \frac{n_A n_B}{1 + \delta_{AB}}, \tag{19}$$

and where $P_s$ is again given by (17). The purpose of deriving Eq. (15), which is an approximate result, along with the exact result (18), is to emphasize the fact that (18) frequently has the behavior of (15). This is important because, in a statistical sampling scheme, far fewer samples are needed to sample a smooth one-dimensional function than for a complex three-dimensional function, assuming the same level of accuracy. In view of the fact that practical considerations often limit one to sample sizes for a single cell ranging from 10 to 100 sample pairs, for each time step, it is clear that such a small sample size is only useful in sampling a smooth one-dimensional function. However, knowing that (18) often has the symmetry of (15), one can operate on (18) with a relatively small sample size and still be confident of obtaining good results. However, for those cases where $F(\boldsymbol{g})$ is believed to be more complex, then it is clear that a larger number of sample pairs is needed for each time step, if one is to obtain reliable results. This situation makes clear where the transition from a general approach characterizing kinetic theory problems to a more restricted approach typically addressed by particle methods is taken.

## IV. SELECTION RULE

In practice, where it is desirable to set the number of particles in a unit cell to as large a value as possible, the corresponding number of possible pairs becomes much too large. For

example, for $n = 100$ we find $S = n^2/2 = 5,000$. Because it is not practical to sample a cell 5,000 times, one must settle for a considerably smaller sample size. If we reduce the size of our sample, $S$, then it is clear that $P_s$ must be increased by a corresponding amount in order for the product to yield the same rate. The approach we will take is that one is free to specify the sample size, $S$, provided that $P_s$ is adjusted to leave the product (15) or (18) unaltered. Because of the adjustment that can be made to the value of $P_s$, we chose to view it as a selection probability as opposed to a collision probability. The concept of a selection probability applies to the model problem, while the concept of a collision probability applies to the original physical problem. On using an arbitrary value of $S$, the corresponding value of the selection probability (17) becomes

$$P_s = \left\{ \frac{n_A n_B}{(1 + \delta_{AB})S} \right\} (\pi d^2) g \Delta t. \tag{20}$$

In the work that follows, we will assume a single specie gas to minimize algebraic complexity. However, the work can be repeated for the case of two species in a straightforward way. Use of $P_s$ in a computational scheme is simplified considerably, if one introduces the definition of the mean-free path length for a hard-sphere molecule and replaces the physical constant $\pi d^2$ by reference values of number density and mean-free path length. This can be done because the hard-sphere relation

$$\lambda = \frac{1}{\sqrt{2}\, n(\pi d^2)}, \tag{21}$$

clearly holds at all points in a flow. This step leads to a more useful expression given by

$$P_s = \left(\frac{n}{2S}\right) \left(\frac{n}{n_{\text{ref}}}\right) \frac{g \Delta t}{\sqrt{2}\, \lambda_{\text{ref}}}. \tag{22}$$

When the simulation of a wind tunnel flow is carried out, freestream conditions may be used to specify the required reference values.

Because the values of $S$ and $P_s$ can be adjusted, it is appropriate to review combinations that lead to optimal computational efficiency. Recognizing that certain data dependencies can eliminate the possibility of exploiting any form of parallelism,[7] we are interested in selecting an algorithmic form that is free of these dependencies. An unfortunate example of such a dependency was identified above in reviewing step (c) of the DSMC time-counter procedure. It is such data dependency that must be avoided if the advantage of parallel

structure is to be gained. Because no single expression adequately covers the concept needed here, we will describe the algorithmic form having the desired properties as being open loop, as opposed to closed loop which requires an input from the state of the system. We turn our attention first to a specification of $S$.

### A. Natural sample size

The principal difficulty in writing efficient code for a computer having a vector or a massively parallel SIMD architecture is introduced by the data dependency associated with step (c). This difficulty can be averted when using selection rule (22) by employing any sample size that is proportional to n, which becomes a natural sample size. For example, $n/2$ sample pairs out of a total of n particles in a unit cell is one such case. Consequently, it proves to be useful to specify the sample size (for a unit volume) as follows

$$S = K\,(n/2), \tag{23}$$

where $K$ is a constant to be determined. Using this value for the sample size, we then have from (22)

$$P_s = \frac{1}{K}\left(\frac{n}{n_{\rm ref}}\right)\frac{g\Delta t}{\sqrt{2}\,\lambda_{\rm ref}}. \tag{24}$$

The advantage introduced by (23) can best be understood as follows. Assume the entire listing of particle data is read sequentially while cell by cell pairings are made of the particles as they occur in the listing. This automatically leads to n/2 pairs, where n is a different number for each cell. For K = 2, the listing is processed twice. However, in order to assure random parings on successive reads, a random entry and a random stride (spacing between entries) is actually used. Here, the number of pairs created is tied directly to the population of a cell and is a number that automatically arises rather than a number imposed on the system. Consequently, selection rule (24) may be applied in step with the processing of the list and one has an open-loop algorithm. We also note that in the application of (24) it is important to use the time averaged value of $n/n_{\rm ref}$, to reduce statistical fluctuations, and therefore it is a known quantity. A discussion of the fact that K need not be an integer value and how that case is handled, together with details on a Cray-2 implementation, can be found in a thesis by McDonald.[8] A straightforward application, without regard to optimization of code performance, is to use (24) in step (iv) to select the pairs that collide.

Clearly Eq. (24) can only be used as a probability when $P_s < 1$, and therefore, any application must account for this restriction. The condition $P_s < 1$ can now be used to fix the minimum permitted value of K, leading to

$$K = \left(\frac{n_{\max}}{n_{\text{ref}}}\right) \frac{g_{\max}\,\Delta t}{\sqrt{2}\,\lambda_{\text{ref}}}. \tag{25}$$

In actual practice the value of $P_s$ is monitored during a simulation to see that it remains less than unity for the conditions used. However, we can judge these conditions by estimating the value of K, which requires that we review the individual quantities appearing in (25). A study of Eqs. (7) and (10) shows that, for an equilibrium gas, 99.4% of the pairs fall in the range $0 \le g \le g_{\max}$, where

$$g_{\max} = 2.5\sqrt{4kT/m}\,. \tag{26}$$

On first sight, it appears that (26) is unbounded, and consequently, (25) would predict an unacceptably large value for $K$ when the flow Mach number is large. However, the temperature does not become unbounded in a simulation, and this can be seen as follows. An estimate for the maximum temperature in a flow can be found by considering the stagnation point on a blunt, adiabatic body in an Euler flow. Along the stagnation streamline, the energy equation leads to the relation

$$a_s^2 = \left(\frac{\gamma - 1}{2} + \frac{1}{M_1^2}\right) u_1^2,$$

where $a_s$ is the speed of sound at the stagnation point, $M_1$ and $u_1$ are the upstream Mach number and fluid speed, respectively, and $\gamma$ is the ratio of specific heats. On combining the last two equations, we obtain an estimate for $g_{\max}$, i.e.,

$$g_{\max} = 5\left(\frac{\gamma - 1}{2\gamma} + \frac{1}{\gamma M_1^2}\right)^{\frac{1}{2}} u_1. \tag{27}$$

This last equation shows that, for a monatomic gas and in the strong shock-wave limit, we have $g_{\max} = \sqrt{5}\,u_1$. Because the quantity $u_1$ is normally set in a simulation, it is easy to see that $g_{\max}$ is roughly twice as large as $u_1$, and therefore, it is not an unbounded quantity, as one would initially be lead to believe on first seeing (26).

Because we will be considering shock-wave profiles in a monatomic gas, we continue with $\gamma = 5/3$ and, in the strong shock-wave limit, Eq. (25) yields the following estimate

$$K \approx 6.3 u_1 \Delta t / \lambda_1,$$

where a density ratio of 4 was used in (25). On the basis of our experience in using the present method, a reasonable value for the dimensionless group corresponds to $u_1 \Delta t/\lambda_1 = 0.15$. This leads to a $K$ value near unity, which is a very practical value. Because the hard-sphere model leads to larger $K$ values than power-law models for realistic gases, we will defer further discussion of this topic until Section V.

### B. Constrained selection probability

If we are interested in a more automatic procedure for limiting the selection probability so that it is always less than unity, then we may make use of the approach introduced by Bird, that is, for the case of the hard-sphere molecule, to set

$$P_s = g/g_{\max}\,, \tag{28}$$

where $g_{\max}$ is the maximum value of the relative speed in the cell. This is the concept employed in step (a) of Bird's time-counter procedure. With this choice, one is assured that the selection probability never exceeds unity. In this case, the sample size is given by

$$S = \frac{n}{2}\left[\left(\frac{n}{n_{\text{ref}}}\right)\frac{g_{\max}\Delta t}{\sqrt{2}\,\lambda_{\text{ref}}}\right]. \tag{29}$$

On comparing the expression in square brackets with the value defined by (25), it is easy to see that the two are directly related, as they must in order to satisfy (18). The most important fact concerning (29) is that the sample size is imposed, as a direct consequence of (28), and therefore the number of times one must carry out step (iv) is set by this value, i.e., one does not have an open-loop algorithm. Because of this, the creation of efficient code for a computer having a vector or a massively parallel SIMD architecture becomes rather difficult when this algorithmic approach is used. Likewise, in the application of (29), one should use the time averaged value of $n/n_{\text{ref}}$ to reduce statistical fluctuations.

### C. Selection rule verification

A straightforward test of the theory is to compare computed shock wave profiles using the present approach with the corresponding profiles predicted by Bird's DSMC method. In order for the comparison to be a rigorous test of the selection rule alone, free of uncontrolled effects, we replaced the time counter procedure used in step (iv), when using the DSMC

method, by selection rule (24) and followed effectively the same series of steps (i) through (vi) in carrying out the simulations. These results therefore do not provide comparative information on vector versus serial code run times. Fig. 3 presents comparisons of shock-wave profiles for Mach numbers of 3 and 10. Both the density and temperature profiles are shown in each case. The simulations employing the present method were carried out using selection rule (24), with $K \approx 1$, $\lambda_1 = 5$ cell lengths, and $u_1 \Delta t = 0.3$ cell lengths. The upstream average particle number density used was approximately 90 particles per cell and the results were time averaged over 1,000 time steps. The DSMC results were obtained from shock-structure data kindly provided by Boyd[9] from his recent work at NASA-Ames Research Center. It is clear from the comparison that the two methods give nearly the same results. This has been found to hold, as well, for other Mach numbers not shown here.

## V. POWER-LAW MOLECULES

All of our results have been developed for the case of a hard-sphere model of molecular interaction. In order to generalize these results, we must return to Eq. (2) and replace the expression for the total collision cross-section for the hard sphere, given by $\pi d_{AB}^2$, by the more elementary form $\sigma(g, \chi)\, d\Omega$, where $\sigma$ is the differential collision cross-section, $\chi$ is the scattering angle, and $d\Omega$ is the differential solid angle. For the hard-sphere model, $\sigma$ is a constant and the scattering is isotropic. For the more general case, one must consider the role played by the scattering angle as well. However, in the application of a particle method, one may first use the integrated collision cross-section, $\sigma_T(g)$, in (2) and then choose the orientation of the relative velocity vector after collision to be a random quantity, selected in correspondence with the scattering properties of the molecular interaction considered. This is where the $\chi$ dependence is introduced, which also explains step (v) in Section II, where the procedural steps in a particle method were outlined. On this basis, we generalize Eq. (2) by replacing the quantity $\pi d_{AB}^2$ by the total collision cross-section $\sigma_T(g)$.

Because the algebraic steps which led from Eq. (2) to Eq. (12) are not affected by the introduction of the function $\sigma_T(g)$, the more general form of (12) can be written immediately as

$$z_{AB}\, d\boldsymbol{g} \Delta t = \left\{ \frac{n_A n_B}{(1 + \delta_{AB})} F(\boldsymbol{g})\, d\boldsymbol{g} \right\} [\sigma_T(g)\, g \Delta t]. \tag{30}$$

The key algebraic step, in developing the dimensionless form (22), was the introduction of the dimensionless group

$$G(g) = \sqrt{2}\, n_{\text{ref}} \lambda_{\text{ref}}\, \sigma_T(g), \tag{31}$$

which was obtained from (21) for the case of a hard-sphere molecule. In anticipation of using the same algebraic step and for the case of a single specie gas, we write Eq. (30) in the form

$$z_{AB}\, d\boldsymbol{g}\Delta t = \left\{\frac{n}{2} F(\boldsymbol{g})\, d\boldsymbol{g}\right\}\left(\frac{n}{n_{\text{ref}}}\right) G(g)\, \frac{g\Delta t}{\sqrt{2}\, \lambda_{\text{ref}}}. \tag{32}$$

The algebraic expression for $P_s$, for the open-loop algorithm, is then obtained directly from (32) and it reads

$$P_s = \frac{1}{K}\left(\frac{n}{n_{\text{ref}}}\right) G(g) \frac{g\Delta t}{\sqrt{2}\, \lambda_{\text{ref}}}. \tag{33}$$

Likewise, by factoring $g\sigma_T(g)/g_{\max}\sigma_T(g_{\max})$ from (32), the sample size S associated with the constrained selection probability is obtained in the same way and is given by

$$S = \frac{n}{2}\left[\left(\frac{n}{n_{\text{ref}}}\right) G(g_{\max}) \frac{g_{\max}\Delta t}{\sqrt{2}\, \lambda_{\text{ref}}}\right]. \tag{34}$$

In the work that follows, we will find a need for a general expression for the mean-free path length in a single-specie gas. The desired relation is found by use of the basic definition

$$\Theta\lambda = \bar{C}, \tag{35}$$

where $\Theta$ is the single-particle collision frequency, and through the definition of the collision frequency expressed in terms of the bimolecular collision rate, given by

$$\Theta = \frac{2}{n}\int_{-\infty}^{\infty} z_{AB}\, d\boldsymbol{g}.$$

The factor of 2 appears because, in the case of like molecules, each collision terminates two free paths.[10] On using (30) for a single specie gas, the single-particle collision frequency is therefore given by

$$\Theta = n\int_{-\infty}^{\infty} g\sigma_T(g) F(\boldsymbol{g})\, d\boldsymbol{g}, \tag{36}$$

which yields the required expression for $\lambda$ when substituted into (35).

A common approach in generalizing hard-sphere results is to assume a repulsive force acting between molecules that is produced by the following potential

$$V = a\, r^{-\alpha}, \tag{37}$$

where $r$ is the distance between the colliding pair, and $a$ and $\alpha$ are constants, characterizing the molecule. The principal problem that arises in using (37) is that its total collision cross-section is infinite for all finite values of $\alpha$. Because of this, the collision frequency and the mean-free path length are not clearly defined for such potentials.

This difficulty has been addressed in several different ways: 1) on the basis of certain physical arguments, a cutoff can be introduced to limit the range of the potential and thus limit the size of the computed quantities; 2) physical arguments can be used to replace the total collision cross-section by either the total cross-section for momentum transfer, $\sigma_M$, or the total cross-section that arises in the calculation of the coefficient of viscosity, $\sigma_\mu$; or 3) use of a novel approach introduced by Bird in which the isotropic scattering of the hard-sphere model is retained, but the molecular diameter is allowed to vary as a function of $g$. This model is called the variable hard-sphere (VHS) model. The argument put forward in favor of the VHS model is the observation that, for most flows of interest, the variation in the collision cross-section has a far greater influence on the structure of a flow than any variation in the molecular scattering characteristics.

### A. Variable hard-sphere model

The variable hard-sphere model was introduced by Bird in 1980, as a practical approach to the solution of engineering problems.[11] Isotropic scattering is assumed, like the hard-sphere model, but its total collision cross-section is allowed to vary with g as follows

$$\sigma_{VHS}(g) = A/g^{2\omega}, \tag{38}$$

where $A$ and $\omega$ are constants. The constant $\omega$ is is related to the exponent of the interaction law (37) by the relation

$$\omega = 2/\alpha. \tag{39}$$

In the development of his model, Bird obtains the following explicit expression for the total

collision cross-section

$$\sigma_T(g) = \sigma_{\text{ref}}[m^* g^2/2(2-\omega)kT_{\text{ref}}]^{-\omega}, \tag{40}$$

which is equation (9) in his paper, and the following expression for the mean-free path length

$$\lambda = (T/T_{\text{ref}})^{\omega}/[(2-\omega)^{\omega}\Gamma(2-\omega)\sqrt{2}\, n\, \sigma_{\text{ref}}], \tag{41}$$

which is equation (10) is his paper. These two equations can be combined to obtain the dimensionless group (31) for the VHS model, which is given by

$$G(g) = \frac{1}{\Gamma(2-\omega)}\left(\frac{2kT_{\text{ref}}}{m^* g^2}\right)^{\omega}, \tag{42}$$

where we note that $m^* = m/2$ for a single specie gas.

On substituting (42) into (33), we obtain the following simple relation for the selection probability for the VHS model

$$P_s = \frac{1}{K}\left(\frac{n}{n_{\text{ref}}}\right) D(\omega)\left(\frac{\bar{C}_{\text{ref}}}{g}\right)^{2\omega} \frac{g\Delta t}{\sqrt{2}\,\lambda_{\text{ref}}}, \tag{43}$$

where the quantity $D(\omega)$ is given by

$$D(\omega) = (\pi/2)^{\omega}/\Gamma(2-\omega). \tag{44}$$

For the case of the hard-sphere molecule, $\alpha = \infty$, or $\omega = 0$, and $\Gamma(2) = 1$; thus $D(0) = 1$ and therefore Eq. (43) reproduces the hard-sphere result (24). For the case of Maxwell molecules, $\alpha = 4$, or $\omega = 1/2$, and $\Gamma(3/2) = \sqrt{\pi}/2$; consequently, $D(1/2) = \sqrt{2}$ and Eq. (40) becomes

$$P_s = \frac{1}{K}\left(\frac{n}{n_{\text{ref}}}\right)\frac{\bar{C}_{\text{ref}}\Delta t}{\lambda_{\text{ref}}}. \tag{45}$$

This last relation shows that, for the case of Maxwell molecules, the bimolecular collision rate is independent of the relative speed $g$, which is a known result. We also note that on comparing (24) and (45) that the quantity $g/\sqrt{2}$ is replaced by $\bar{C}_{\text{ref}}$, which is a much smaller quantity when the Mach number is large. Therefore, the condition $P_s < 1$ is much easier to satisfy for Maxwell molecules than for hard-sphere molecules.

## B. Cross-section for momentum transfer

An alternative to using the constants implied by (40) is to assume that one may use the collision cross-section for momentum transfer given by[12]

$$\sigma_M(g) = 2\pi \left(\frac{2\alpha a}{m}\right)^{2/\alpha} g^{-4/\alpha} A_1(\alpha), \tag{46}$$

where $\alpha$ and $a$ are the constants appearing in (37) and the quantity $A_1(\alpha)$ is a pure number, for which tabulated values (where $\nu = \alpha + 1$) can be found in Chapman and Cowling.[13] The collision cross-section for momentum transfer reduces to the hard-sphere value when $\alpha = \infty$, and therefore, it is more suitable for use here than the cross-section associated with the coefficient of viscosity, which reduces to 2/3 of the hard-sphere value. On comparing (46) and (40), it is clear the two functional forms are identical, except possibly for the constants.

In order to compute the dimensionless group (31), we need an expression for the mean-free path length at the reference conditions. This is where (35) and (36) prove useful. On substituting (46) into (36), assuming the equilibrium state (7) and using definition (10), we obtain

$$n_{\text{ref}}\Theta_{\text{ref}} = \left\{2\pi \left(\frac{2\alpha a}{m}\right)^{2/\alpha} A_1(\alpha)\right\} \frac{4}{\sqrt{\pi}} \left(\frac{4kT_{\text{ref}}}{m}\right)^{\frac{1}{2}-\frac{2}{\alpha}} \Gamma(2 - \frac{2}{\alpha}). \tag{47}$$

Equations (46) and (47) can now be used to eliminate the collection of constants grouped within the braces in (47) to obtain an expression relating $n_{\text{ref}}\Theta_{\text{ref}}$ and $\sigma_M(g)\, g^{\frac{4}{\alpha}}$. Finally, on using (35) to introduce the mean-free path length, and (31) to obtain the dimensionless group $G(g)$, we obtain

$$G(g) = \frac{1}{\Gamma(2 - \frac{2}{\alpha})} \left(\frac{4kT_{\text{ref}}}{m\, g^2}\right)^{\frac{2}{\alpha}}. \tag{48}$$

On using (39) it is clear that (48) and (42) are identical, and therefore, the exact same selection rule is obtained for the two models, i.e., Eq. (43) applies to both cases.

## C. Sample size

Because the two models predict exactly the same results for $G(g)$ and Eq. (43) applies to both models, the sample size for each is obtained from (43) and we have

$$K = \left(\frac{n_{\text{max}}}{n_{\text{ref}}}\right) D(\omega) \left(\frac{\bar{C}_{\text{ref}}}{g_{\text{max}}}\right)^{2\omega} \frac{g_{\text{max}} \Delta t}{\sqrt{2}\, \lambda_{\text{ref}}}. \tag{49}$$

In order to study this equation, we need an estimate for the quantity $\bar{C}_{\mathrm{ref}}/g_{\mathrm{max}}$. This can easily be obtained from the definitions for $\bar{C}$, given by (14), the definition for the Mach number, and by use of Eq. (27), which lead to

$$\frac{\bar{C}_{\mathrm{ref}}}{g_{\mathrm{max}}} = \frac{2}{5}\sqrt{\frac{2\gamma}{\pi}}\left(1+\frac{\gamma-1}{2}M_1^2\right)^{-\frac{1}{2}}. \tag{50}$$

A better estimate for the ratio $n_{\mathrm{max}}/n_{\mathrm{ref}}$, than the constant used in Section IV, is to use the stagnation-point density, as a function of the upstream Mach number. After these equations are collected, the resulting expression for $K$ becomes sufficiently lengthy that a graphical display of the results becomes more appropriate than an algebraic display of the resulting equation.

Fig. 4 presents the functional dependence of $K$ on the power-law constant $\omega$, for fixed values of upstream Mach number $M_1$, and for $\gamma = 5/3$. In evaluating (49) the dimensionless quantity $u_1\Delta t/\lambda_1$ was assigned the value 0.3, which we have found to be a reasonable value. Typical values for $\omega$ for physical gases fall in the mid range of the $\omega$-values plotted. For example, $\omega \approx 0.25$ for the monatomic gas argon, while $\omega \approx 0.22$ for the diatomic gas nitrogen. It is clear from the figure that for physical gases we may use $K$ values near unity and that the situation even improves as the freestream Mach number increases. It is also clear that the hard-sphere model ($\omega = 0$) represents the most severe case, while the Maxwell molecule ($\omega = 0.5$) represents the least severe case.

A study of Eq. (49), and the plot in Fig. 4, show that the sample size, $K$, is more sensitive to the density than to the temperature in the flow. Our estimates were made for the stagnation point of a blunt body and a thermally insulated wall. If the wall were a cold wall, then the temperature of the gas at the stagnation point would be low, but its density would be high. It is extremely difficult to obtain general analytic results for this case, but several exploratory runs seem to indicate that the net effect is to increase the value of $K$ by as much as 50%, over those found in Fig. 4, when the Mach number reaches 30. However, the figure shows that $K = 2$ would also handle this case for typical physical gases, and therefore, the basic approach is the same.

Equation (43) gives the selection rule for the open-loop algorithm for either the VHS model or for the model using the collision cross-section for momentum exchange. We found in Section IV that the hard-sphere limit of this selection rule predicts the same shock-wave

profiles as those given by Bird's DSMC method. A further test of the present approach is to study the opposite limit, namely, the Maxwell molecule limit. The selection rule for the open-loop algorithm has already been derived for this case, and it is given by Eq. (45). Fig. 5 presents comparisons between the shock-wave profiles obtained using (45) and results from the DSMC method, for the case of Maxwell molecules, a monatomic gas, and for the shock-wave Mach numbers of 3 and 10. In our simulations, we used $K \approx 1$, $\lambda_1 = 1.5$ cell lengths, and $u_1 \Delta t = 0.3$ cell lengths. The upstream average particle number density used was approximately 110 particles per cell and the results were time averaged over 1,000 time steps. It is quite evident from the comparisons that there is essentially complete agreement between the two methods. The DSMC results were again obtained by making use of shock-structure data provided by Boyd.[9]

The shock wave provides a test for a nonequilibrium gas, while an appropriate test for an equilibrium gas is to compare the collision frequency, or mean free path length, in a single cell with the predictions of kinetic theory. Equation (41) shows that $\lambda$ varies as $T^{1/2} n^{-1}$ for a Maxwell molecule and as $n^{-1}$ for a hard sphere molecule. Because the former represents the more rigorous test, we show in Fig. 6 the results of several example simulations for $\lambda$ versus n for two values of the sound speed, differing by an order of magnitude, and for a range of densities representative of many simulations of interest. It can be seen that the comparison is quite good, which further supports the view that the proposed selection rule is valid.

### D. Time-counter method

Because the shock-wave profiles predicted by the present theory are essentially identical to the profiles predicted by the DSMC method, it is clear that the two approaches must be closely related. The comparison that suggests itself next is to consider whether Eq. (30), which is the central equation in the application of our method, can be related to the time-counter procedure in the DSMC method.

If we cancel the $\Delta t$ in (30), assume a single specie gas and integrate over $\boldsymbol{g}$, we obtain the relation

$$Z_{AB} = \frac{n^2}{2} < g \sigma_T(g) >, \tag{51}$$

where $Z_{AB}$ is the integrated bimolecular collision rate and the operator representing the mean quantity is defined by

$$< g\sigma_T(g) > = \int_{-\infty}^{\infty} g\sigma_T(g)F(\boldsymbol{g})\, d\boldsymbol{g}. \tag{52}$$

If $V$ is defined to be the volume of a small element in physical space, then the quantity

$$\tau = 1/(VZ_{AB}), \tag{53}$$

represents the average time between binary collisions in the volume $V$. On substituting (51) into (53) and defining the number of particles in the small volume to be $N = Vn$, we have

$$\tau = \frac{2}{Nn < g\sigma_T(g) >}. \tag{54}$$

The average number of binary collisions, $N_{coll}$, occurring in the volume $V$ in the time $\Delta t$ is given by $N_{coll} = \Delta t/\tau$ and therefore (54) can be arranged to read

$$\Delta t = N_{coll}\left(\frac{2}{Nn < g\sigma_T(g) >}\right). \tag{55}$$

Turning our attention to the time-counter method and steps (a), (b) and (c), the sum represented by step (c) can be written for a single time step, $\Delta t$, as follows

$$\Delta t = \sum_{i=1}^{N_{coll}} \left(\frac{2}{Nng\sigma_T(g)}\right)_i, \tag{56}$$

where $N_{coll}$ is the same quantity introduced in (55). Now, the operator representing the mean quantity appearing in the denominator of (55) is based on the distribution $F(\boldsymbol{g})$, as defined by (52). However, the statistical sampling procedure used in steps (a), (b) and (c) does not lead to a mean based on $F(\boldsymbol{g})$, because the filtering action of step (a) modifies the distribution to one that is proportional to $g\sigma_T(g)F(\boldsymbol{g})$. Identifying this modified distribution by the symbol $F_c(\boldsymbol{g})$, its representation in normalized form is therefore given by

$$F_c(\boldsymbol{g}) = \frac{g\sigma_T(g)F(\boldsymbol{g})}{< g\sigma_T(g) >}. \tag{57}$$

On this basis, the sum in (56) is described by the following mean quantity

$$\Delta t = N_{coll}\left\langle \frac{2}{Nng\sigma_T(g)} \right\rangle_{F_c}, \tag{58}$$

where the mean is based on the distribution $F_c(\boldsymbol{g})$ and the operator used in (58) is defined by

$$\left\langle \frac{2}{Nng\sigma_T(g)} \right\rangle_{F_c} = \int_{-\infty}^{\infty} \left( \frac{2}{Nng\sigma_T(g)} \right) F_c(\boldsymbol{g})\, d\boldsymbol{g}. \tag{59}$$

Noting the cancellation that occurs when (57) is substituted into (59) and the fact that $F(\boldsymbol{g})$ is a normalized distribution, we see that Eq. (58) reduces to

$$\Delta t = N_{coll} \left( \frac{2}{Nn < g\sigma_T(g) >} \right), \tag{60}$$

which is exactly the same as Eq. (55). Therefore, the two approaches are entirely equivalent, which explains why the comparisons of shock-wave profiles resulted in such close matches.

The key step connecting the two methods is the relation between the operators appearing in (55) and (58), i.e.,

$$\frac{1}{< g\sigma_T(g) >_F} = \left\langle \frac{1}{g\sigma_T(g)} \right\rangle_{F_c}. \tag{61}$$

This is a general result, which can be derived on the basis of probability theory alone, and it does not depend on the particular function $g\sigma_T(g)$ used here. Because the mean and reciprocal operators do not commute, Eq. (61) is needed to make the proper transformation.

## VI. DISCUSSION AND CONCLUSIONS

The key equation in the application of the present method is Eq. (30). It gives the number of $AB$ collisions occurring in a unit volume, in a specific relative-velocity range, in the time $\Delta t$. The selection rule for the open-loop algorithm which follows from this equation, for the case of a single specie gas and the VHS model, or the model using the collision cross-section for momentum exchange, is given by Eq. (43). Additionally, the corresponding equation for the appropriate sample size, used with the selection rule, is given by Eq. (49). The basic difference between the present method and the DSMC method is in the application of step (iv). Briefly, in the present method, the list of particle data is processed K times, automatically creating S = K(n/2) random sample pairs, where n is a different number for each cell. On using selection probability (43) in step with the processing of the list, to determine which pairs collide in each cell, the resulting collisions then satisfy (30) in terms of the number of collisions per unit volume in the time $\Delta t$ and in the distribution over relative

velocity $\boldsymbol{g}$. The sole interest in the present method is that it leads to an open-loop algorithm and greater computational efficiency on certain machines, as opposed to the closed-loop sequence of steps required by the time counter method described by the three operations (a) through (c). The discussion following Eq. (24) should be consulted for a more precise description of the method.

The aim of our discussion has been to first establish the validity of the proposed selection rule, and not on a comparison of execution speeds for different computer codes. The extensive programming details used in implementing the present theory on the Cray-2 supercomputer is presented in Ref. 8 and will not be reviewed here. Nevertheless, the presentation of several example cases representing the capability of the method are appropriate, in order to establish that the method does in fact offer a computational capability which has not existed before.

Figs. 7, 8 and 9 present three such examples. In each of these cases, the flow was simulated as a three-dimensional flow, even when the intent was to study a two-dimensional problem. Also, all the cases represent an ideal diatomic, hard-sphere gas with an adiabatic, no-slip boundary condition on the body surface. The Knudsen number in each case was chosen to be reasonably small so that near-continuum flow would be realized. The sample size $K \approx 1$ together with the parameter $u_1 \Delta t = 0.3$ cell lengths were used in all three cases. In addition, all the simulations were carried out using cubical, three-dimensional unit cells everywhere in space. This we consider to be a very important component in producing code that executes very quickly. All the simulations were carried out on the NAS Cray-2 at NASA-Ames Research Center.

Fig. 7 presents the results of a simulation for a Mach 6 flow about a circular cylinder. The simulated wind tunnel consisted of a space of 120 cells high, 80 cells long and 3 cells deep, and the circular cylinder was 40 cells in diameter. The Reynolds number based on the diameter was 720. The simulation was carried out using $1.0 \times 10^6$ particles and $\lambda_1 = 0.5$ cell lengths. The figure shows the density distribution in the flow, where the display is in the form of an infinite fringe interferogram. The interest in the problem was in determining whether the correct shock-wave detachment distance would be predicted by the simulation. This was found to compare very favorably with experiment, giving confidence in the programming and the simulation method used. The simulation was carried out using a full cylinder and therefore the symmetry seen in the flow gives further confirmation of the method employed.

Fig. 8 represents a simulation for a Mach 6 flow about a 10 degree half-angle wedge, where the velocity vector field is displayed. The dimensions of the simulated flow were 90 cells high, 256 cells long and 3 cells deep. The wedge was 128 cells long and 22 cells high; and based on the full base height, the Reynolds number was 1760. In this case a total of $0.74 \times 10^6$ particles were used in the simulation with $\lambda_1 = 0.23$ cell lengths. The aim of the investigation was to see how detailed the resulting velocity field would be. Of great interest is the detail found in the structure of the boundary layer on the wedge surface and in the detail found in the region immediately behind the wedge. The vortex flow behind the wedge can be seen very clearly, if the scale of the flow is increased to allow one to focus on it. This result contradicts the conclusion drawn by Meiburg[14] who argued that the molecular-dynamics method of particle simulation must be employed in order to see such phenomena. Additional flow detail which can be seen more clearly in the pressure field than in the velocity field is the existence of a wake shock.

Fig. 9 presents the results of a study of a true three-dimensional simulation, and represents an attempt to learn how well a three-dimensional flow can be resolved with the capability at hand. The simulated wind tunnel consisted of a space of 120 cells high, 60 cells long and 60 cells deep. A total of $9.5 \times 10^6$ particles were used in the simulation. The body diameter was 44 cell lengths, $\lambda_1 = 1.0$ cell lengths, and $M_1 = 35$. The Reynolds number based on the body diameter was 2300. The view shown is the pressure field in the central plane of a blunt nosed body inclined at an angle with respect to the freestream. The body represents a typical blunt shape being considered for use on spacecraft for aerodynamically assisted orbital changes. These results were obtained as part of a study at NASA-Ames Research Center to apply the methods discussed above to practical aerospace problems.[15]

All of the above cases were run at a program execution rate of around 1 to 2 $\times 10^{-6}$ seconds per particle per time step. For a simulation employing $10^6$ particles, approximately 1 to 2 seconds of computation time is required per time step. Because a statistical method requires time averaging over many time steps, to reduce statistical fluctuations in the results, the total run time depends directly on the length of time averaging employed; thus, the use of roughly 1,000 time steps leads to approximately one-half hour of Cray-2 computation time.

## ACKNOWLEDGEMENTS

We would like to express our appreciation to I. D. Boyd who kindly made available shock-wave data obtained from his DSMC simulations, which were used in the shock-wave profile comparisons, and for his helpful discussions.

This work was supported by the National Aeronautics and Space Administration under Grant No. NCA2-313, by the Air Force Office of Scientific Research under Grant No. AFOSR 88-0139, and in part by Hypersonics Research and Training Grant No. NAGW-965. All of the computational work carried out on the NAS Cray-2 supercomputer was supported by NASA-Ames Research Center.

## References


[1] G. A. Bird, *Molecular Gas Dynamics*, (Clarendon Press, Oxford, 1976).

[2] G. A. Bird, Ann. Rev. Fluid Mech. **10**, 11 (1978).

[3] H. Ploss, Computing **38**, 101 (1987).

[4] See Ref. 1, p. 6 and p. 212.

[5] W. G. Vincenti and C. H. Kruger, *Introduction to Physical Gas Dynamics*, (Wiley, New York, 1965).

[6] J. L. Melsa and A. P. Sage, *An Introduction to Probability and Stochastic Processes*, (Prentice-Hall. New Jersey, 1973), Sec. 7.3.

[7] D. A. Padua and M. J. Wolfe, Comm. of the ACM **29**, 1184 (1986).

[8] J. D. McDonald, Ph.D. thesis, Stanford University, 1989.

[9] I. D. Boyd (private communication).

[10] See Ref. 5, Chap. II, Sec. 6.

[11] G. A. Bird, in *Rarefied Gas Dynamics: Technical Papers from the 12th International Symposium*, Progress in Astronautics and Aeronautics Series (AIAA, New York, 1980) **74**, Part 1, p. 239.

[12] See Ref. 5, Chap IX, Sec. 8.

[13] S. Chapman and T. G. Cowling, *The Mathematical Theory of Non-Uniform Gases*, (Cambridge University Press, London, 1952), Sec. 10.3.

[14] E. Meiburg, Phys. Fluids **29**, 3107 (1986).

[15] W. J. Feiereisen (private communication).

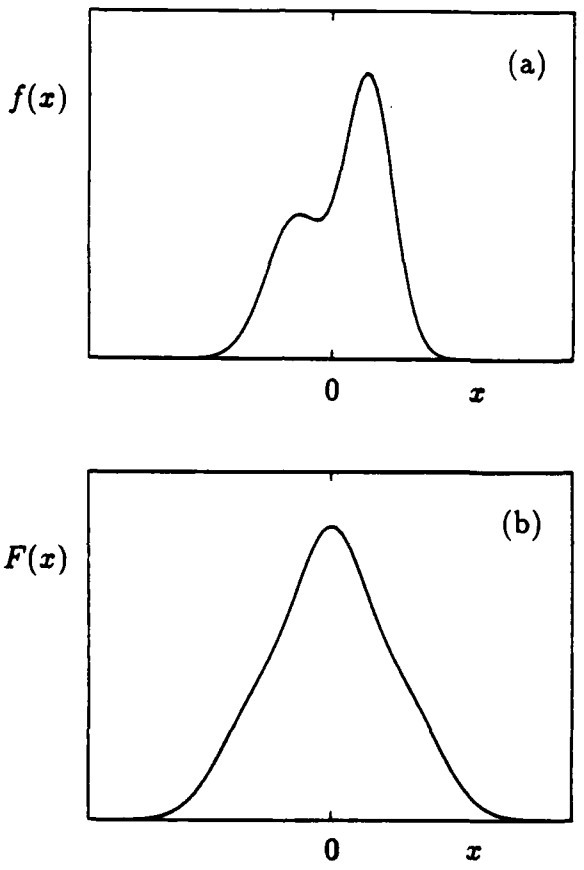


Fig. 1. A study of the properties of Eq. (9). (a) An assumed bimodal distribution for $f$. (b) The function $F = f\#f$.

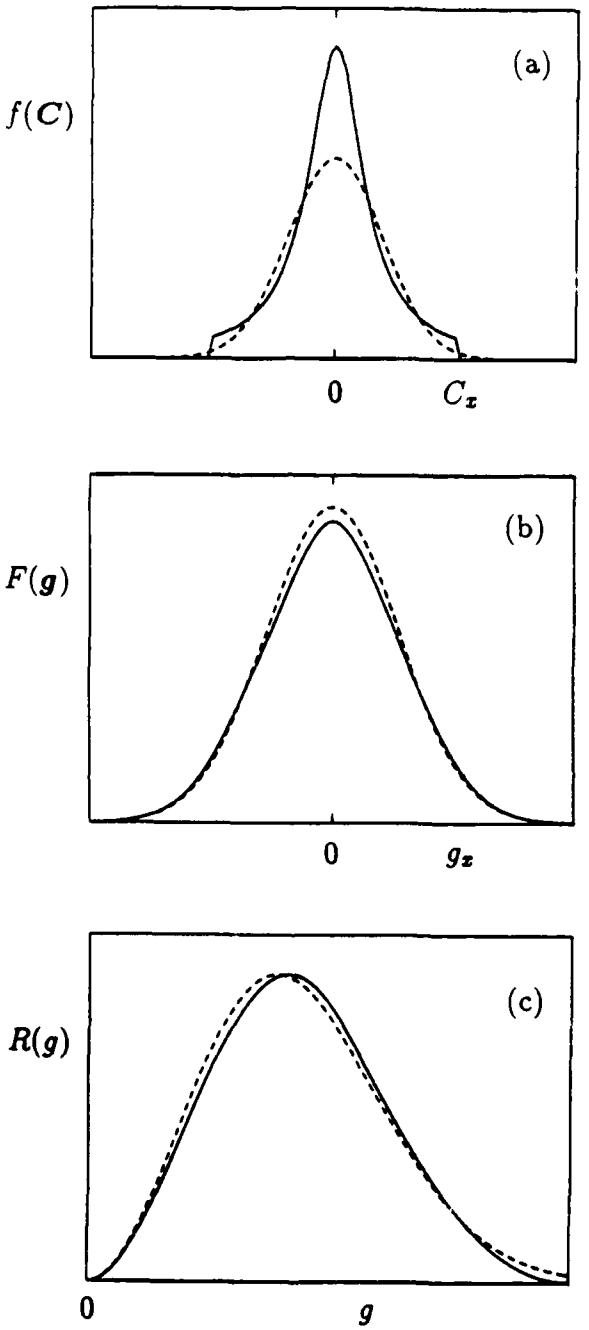


Fig. 2. A study of the properties of Eq. (5). (a) An assumed spherically symmetric, truncated Cauchy distribution. (b) The function $F(g)$ . (c) The function $R(g)$. ____, test function; _ _ _ _, equivalent Maxwellian.

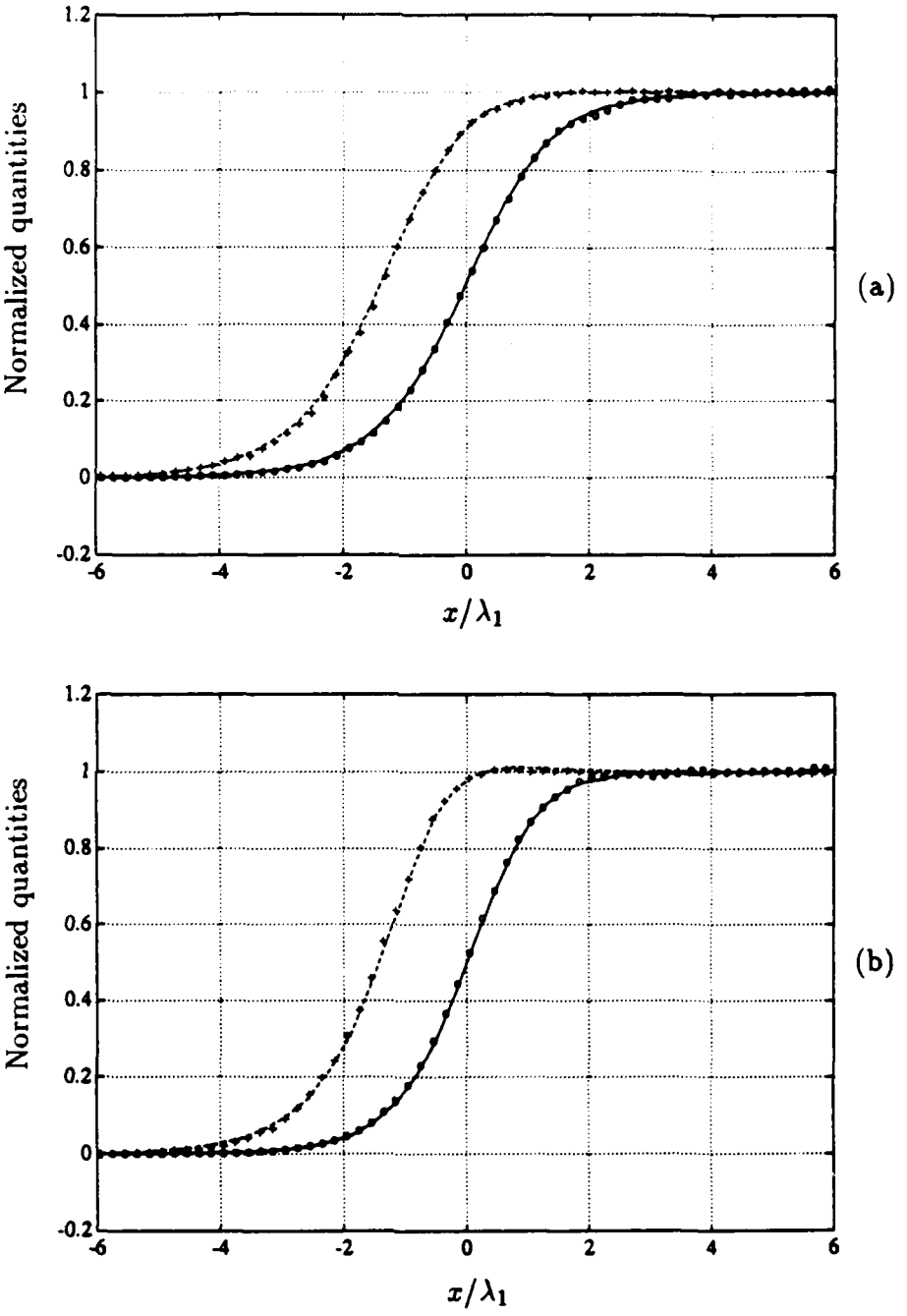


Fig. 3. Shock-wave density and temperature profiles for a monatomic, hard-sphere gas. The symbols designate the solution obtained using selection rule (24) and the solid (density) and dashed (temperature) curves are for the DSMC method (Ref. 11). (a) $M_1 = 3$. (b) $M_1 = 10$.

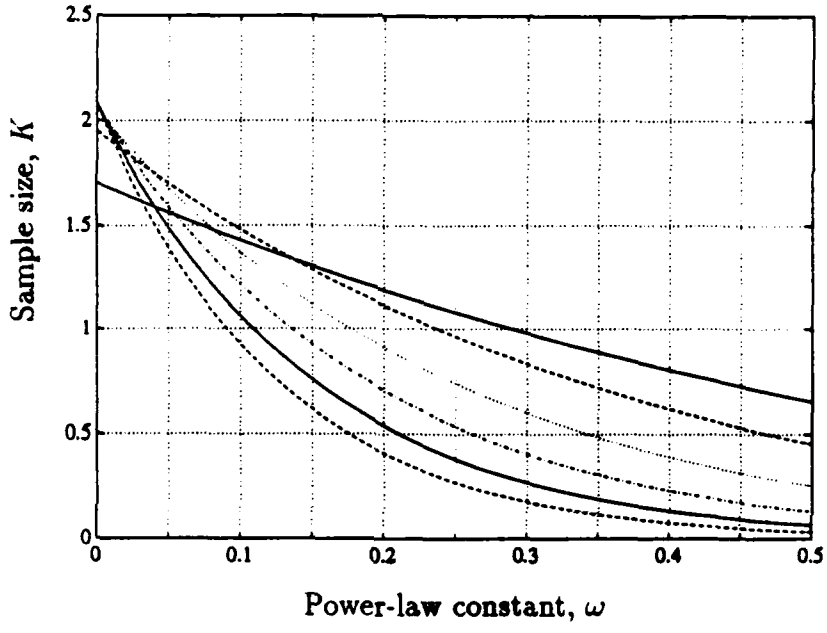


Fig. 4. Functional dependence of the sample size $K$ on the power-law constant $\omega$ and the freestream Mach number $M_1$, for the case $\gamma = 5/3$ and $u_1 \Delta t / \lambda_1 = 0.3$. $M_1 = 2$ (solid line), 4, 8, 16, 32, 64 (dashed line).

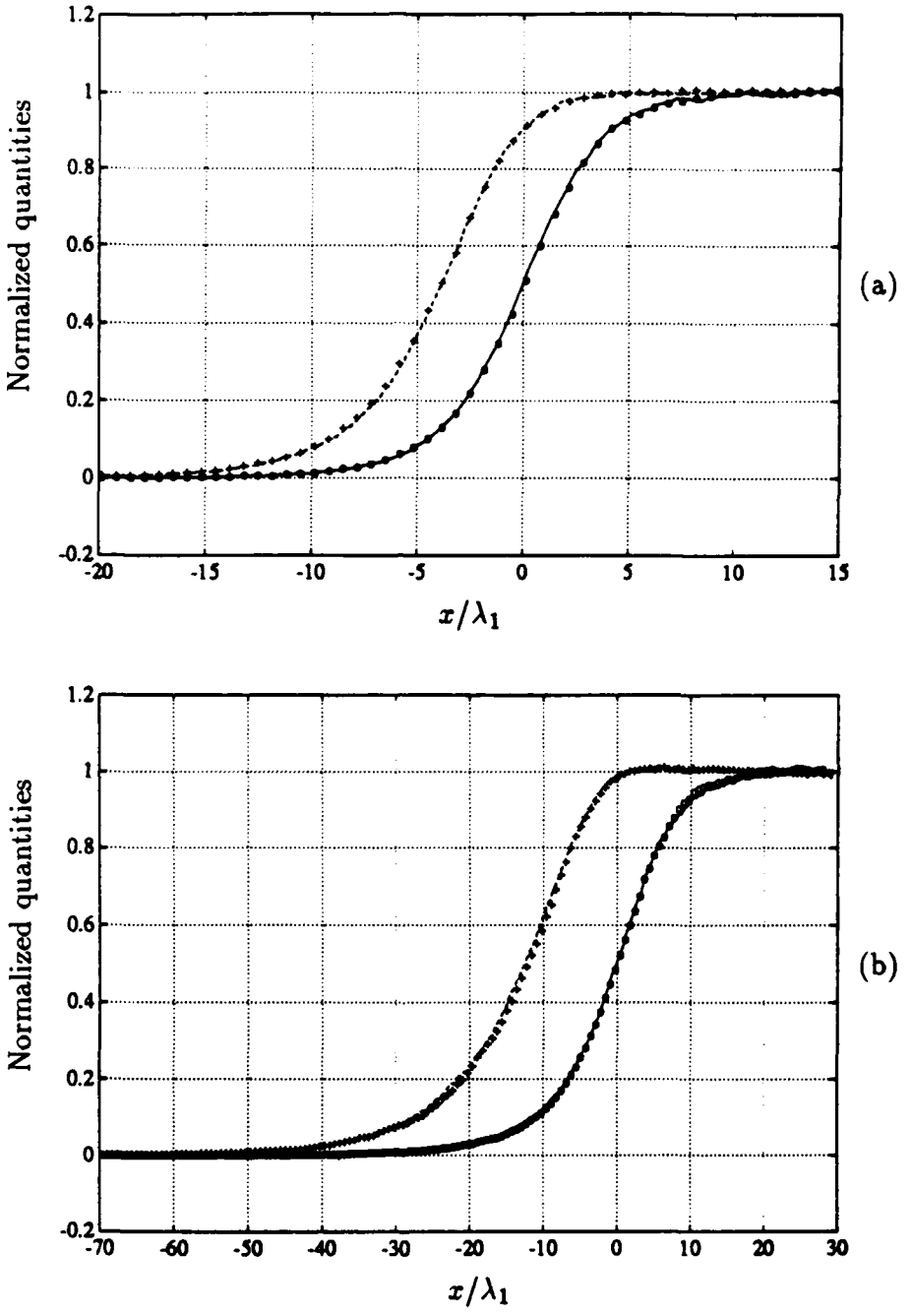


Fig. 5. Shock-wave density and temperature profiles for a monatomic, Maxwell-molecule gas. Symbols designate the solution obtained using Eq. (45) and the solid (density) and dashed (temperature) curves are for the DSMC method (Ref. 11). (a) $M_1 = 3$. (b) $M_1 = 10$.

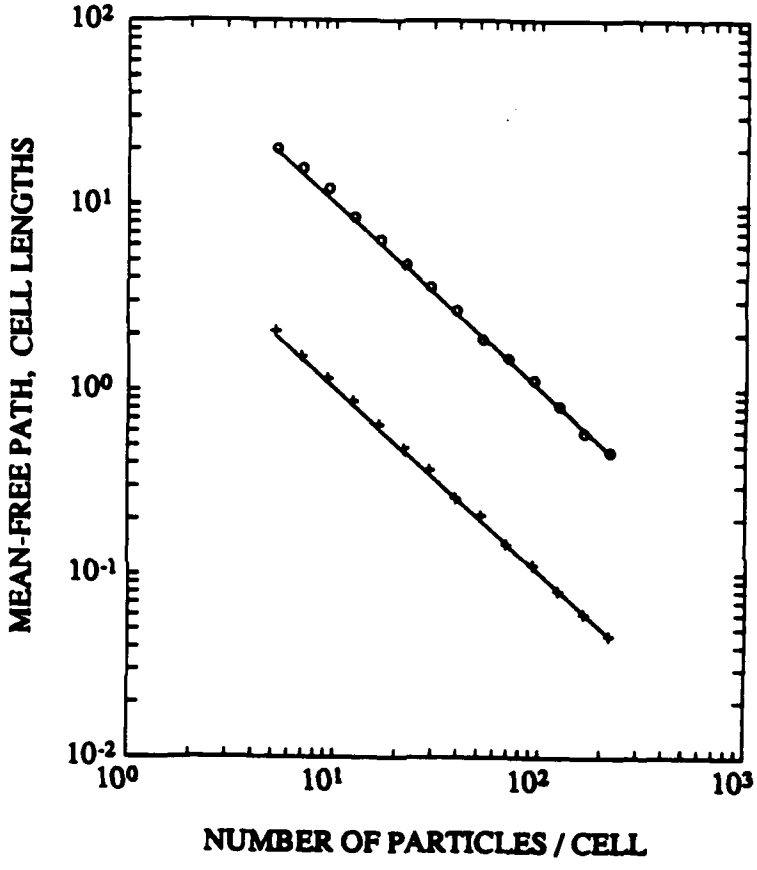


Fig. 6. Comparisons of the mean-free path length obtained in simulations based on selection rule (45) for Maxwell molecules and with kinetic theory. Sound speed (cell lengths/time step): o, 0.2; +, 0.02.

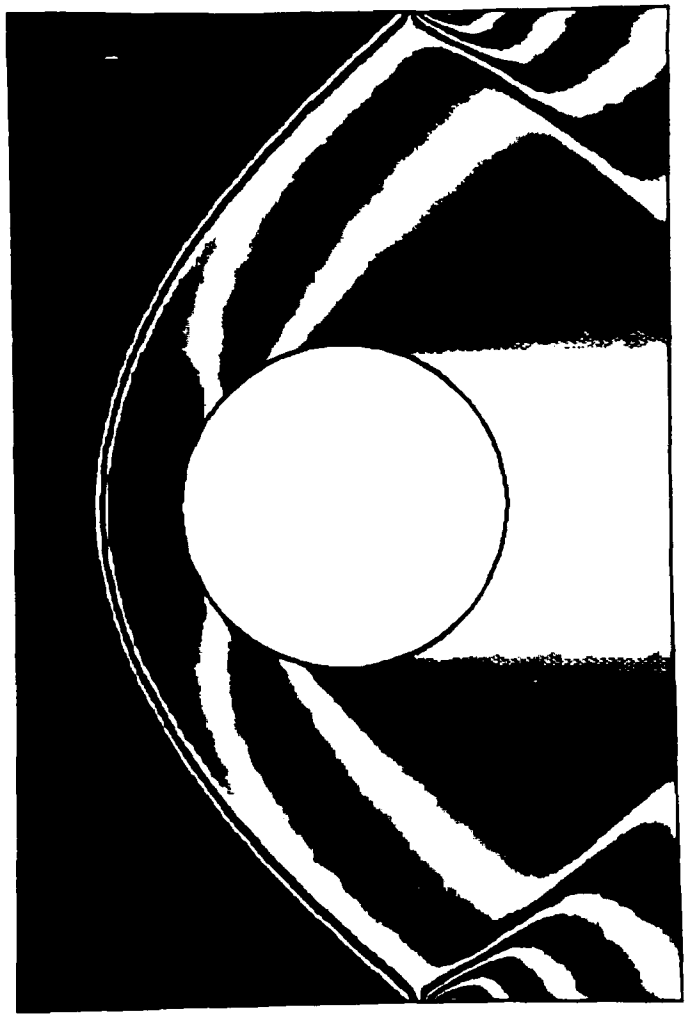

Fig. 7. Flow past an adiabatic circular cylinder for the case of a hard-sphere, diatomic gas and a Mach number of 6. Density distribution is shown in the form of an infinite fringe interferogram. A total of $1.0 \times 10^6$ particles in a space of $120 \times 80 \times 3$ cells were used in the simulation.

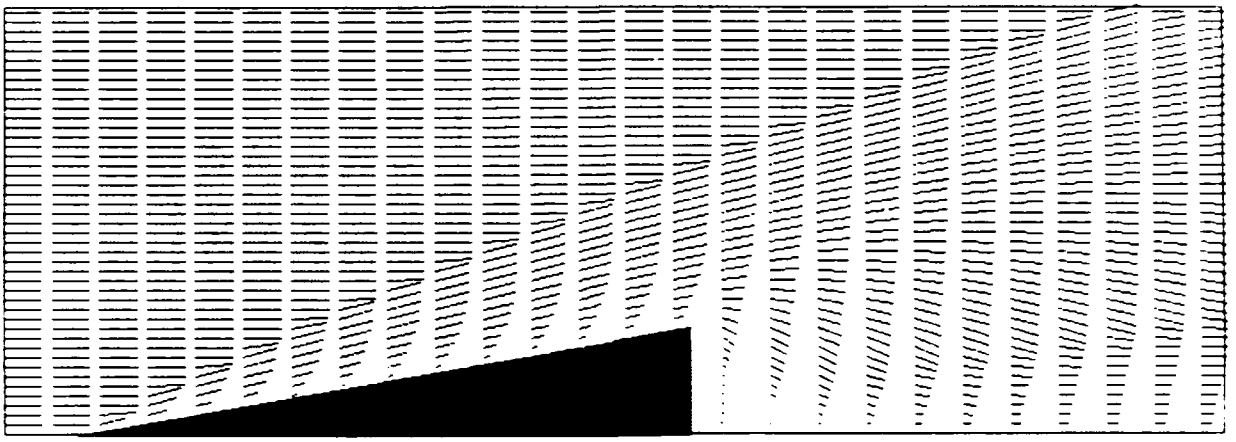

Fig. 8. Velocity vector field about an adiabatic, 10 degree half-angle wedge for the case of a hard-sphere, diatomic gas and a Mach number of 6. A total of $0.74 \times 10^6$ particles in a space of $90 \times 256 \times 3$ cells were used in the simulation.

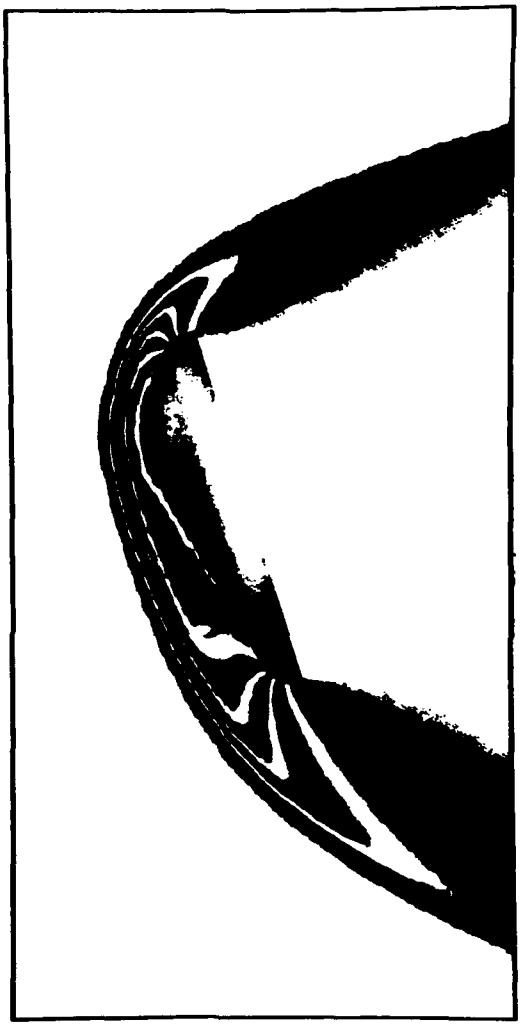

Fig. 9. Pressure distribution in the central plane of a three-dimensional Mach 35 flow described in the text. A total of $9.5 \times 10^6$ particles in a space of $120 \times 60 \times 60$ cells were used in the simulation. The body diameter was 44 cell lengths and $\lambda_1 = 1.0$ cell lengths.

# APPENDIX B

# FUNDAMENTALS OF CHEMISTRY MODELING APPLICABLE TO A VECTORIZED PARTICLE SIMULATION

Brian L. Haas*

Department of Aeronautics and Astronautics
Stanford University
Stanford, California 94305

## ABSTRACT

The flowfield about vehicles re-entering the atmosphere is characterized by hypersonic rarefied flow in thermochemical non-equilibrium. An appropriate method for computing such flows is direct particle simulation, an efficient implementation of which utilizes the vector-processing capability of current supercomputers. The fundamentals of extending the vectorized simulation to model chemically reactive flows are described here. A review is presented of the reaction physics of dissociation, exchange reactions, and recombination, with attention to internal energy mode contribution. Reaction selection rules, as functions of reactive collision energy, are reviewed. Reaction mechanics modeling is constrained by considerations of detailed balance at equilibrium, and conservation of linear momentum and energy. The proposed means of partitioning post-reaction energy among the energy modes of the products is based on proportional energy exchange per mode. Details of reaction mechanics per reaction are presented with particular attention to the quantum nature of the vibrational mode. Verification of the models is made through simulation of superheated diatomic reservoirs relaxing thermochemically to equilibrium.

## NOMENCLATURE

| | |
|---|---|
| $A, B, C, \ldots$ | monatomic chemical species |
| $AB, AC, \ldots$ | diatomic chemical species |
| $n$ | number density |
| $k_f$ | forward rate coefficient |
| $K$ | equilibrium concentration coefficient |
| $k$ | Boltzmann's constant |
| $T$ | temperature |
| $\mu$ | reduced mass of colliding pair |
| $\alpha$ | exponent in power law potential |
| $\sigma$ | constant in collision probability |
| $g$ | relative speed of collision |
| $a$ | constant in Arrhenius expressions |
| $b$ | exponent in Arrhenius expressions |
| $\mathbf{x}$ | position of a particle |
| $\mathbf{u}$ | velocity of a particle |
| $\mathbf{G}$ | collision center-of-mass velocity |
| $E_d$ | activation energy for reaction |
| $\epsilon, \varepsilon, \xi$ | energies |
| $P$ | probability |
| $f$ | energy distribution function |
| $\zeta$ | number of degrees of freedom |
| $\theta_v$ | vibrational characteristic temperature |
| $\beta$ | constant in reaction probability |
| $\psi$ | exponent in $P_d$ function |
| $\phi$ | exponent in $P_r$ function |
| $\Delta_d$ | degree of dissociation |
| $\Re$ | uniform random number |
| $q, i, j$ | vibrational quantum levels |
| $Q$ | maximum quantum level |

Superscripts:

| | |
|---|---|
| $'$ | post-collision value |
| $''$ | post-dissociation value |
| $*$ | equilibrium value |

Subscripts:

| | |
|---|---|
| $a, b$ | pair of species $a$ and $b$ |
| $AB$ | collision pair, $A$ and $B$ |
| $(AB), o$ | orbital-pair for $A$ and $B$ |
| $X$ | collision partner of any type |
| $c$ | collision |
| $d$ | dissociation |
| $r$ | recombination |
| $f$ | denotes forward reaction rate |
| $e$ | denotes equilibrium concentration |
| $int$ | internal energy modes |
| $rel$ | relative translational mode |
| $rot$ | rotational mode |
| $vib, v$ | vibrational mode |
| $3, 4$ | reactions in equations 3 and 4 |
| $m$ | energy mode |
| $rev$ | reverse reaction |
| $ref$ | reference value |

## INTRODUCTION

Potential development of vehicles such as the National Aerospace Plane (NASP) and the Aeroassist Flight Experiment (AFE) have renewed interest in modeling hypersonic rarefied flow. Such flows may be characterized by non-equilibrium between molecular energy modes and between the concentrations of

* Research Assistant, Student Member, AIAA

different species in the rarefied gas. Temperatures exceeding $20,000K$ are possible behind the leading shock of a vehicle entering the atmosphere with near-orbital velocity. Such conditions excite the vibrational mode of molecules in the air leading to dissociation. Exchange reactions and recombination of free atoms will occur near cold catalytic surfaces and during expansion of the gas around body shoulders. The finite rates of thermal excitation and reaction processes significantly alter the character of the flowfield, affecting the temperatures, pressures, and heat-transfer experienced by the body, and thus dramatically influencing the aerodynamics of the vehicle.

The degree of rarefaction of these flows, at altitudes above 80km, is characterized by Knudsen numbers exceeding 0.01. The low-density nature of this flow is such that the familiar Navier-Stokes equations are not applicable due to failure of the linear constitutive relations. In contrast, discrete particle methods are based on real-gas molecular models and provide potentially powerful alternatives for simulating these flows. One frequently-applied particle simulation is the Direct Simulation Monte Carlo (DSMC) method of Bird which, in a recent form[1], is capable of solving only modest-sized problems due to large computational requirements. An alternate particle simulation method developed by Baganoff and McDonald[2-5] is structured specifically for the vector-processing architectures of current supercomputers, resulting in significant improvement in performance. Current implementation of that simulation models the three dimensional non-reactive flow of general gas mixtures[4].

This paper introduces the fundamentals of extending this vectorized particle simulation to treat chemically reacting flows. Comprehensive modeling of chemical kinetic processes in a gas involves solution of the Schrödinger wave equation, and is therefore ill-suited for large-scale simulations. However, meaningful simulations can be obtained by developing reaction models, applied at the particle collision level, which yield the correct macroscopic chemical behavior. The types of particles used in the simulation and their properties are presented along with a review of chemical reactions. The basics of vector processing are introduced with a brief description of how the simulation is structured to be compatible with them, including discussion of the mechanics of thermal collisions. The reaction selection rules, based on reaction probabilities as functions of collision energy, are then reviewed. Reaction mechanics are presented, with details of how post-reaction energy is partitioned among the energy modes of the products. The thermochemical model is then applied to a reservoir of superheated diatomic molecules relaxing thermally and chemically to equilibrium, demonstrating its ability to simulate reactive flows.

## REACTION PHYSICS

Atmospheric air, under the hypersonic conditions described, can be approximately modeled by the following five-species set: $O_2$, $N_2$, $NO$, $O$, and $N$. A more complete model would include some of the ions such as $NO^+$. Associated with each particle in the flow is its position, $\mathbf{x} = (x, y, z)$; its velocity, $\mathbf{u} = (u, v, w)$; its species-type; and the energy of its internal modes, $\epsilon_{rot}$ and $\epsilon_{vib}$ if it is diatomic. Each species is identified by its mass, relative diameter, and characteristic temperatures of vibration and dissociation.

Associated with the species set are 15 dissociation/recombination reactions, and 4 exchange reactions suggested by Bird[6] and listed in Table 1. Included in the table are the parameters pertaining to the macroscopic reaction rate coefficients, $k_f(T)$, and the species concentration coefficients, $K(T)$[7], obtained by fitting experimental data to Arrhenius form. Although application of this experimental correlation for temperatures exceeding 10,000K is questionable, it is used here for lack of a better alternative. The reaction selection rules are derived to reproduce the macroscopic temperature-dependence given by the Arrhenius forms.

Very little is understood regarding the non-equilibrium behavior of a chemically reacting gas. However, reaction rates and concentrations are well documented for gases very near equilibrium. Therefore, to model non-equilibrium flow we must devise reaction models based upon our limited knowledge of the microscopic physics, specifying the unknown parameters of those models by matching the experimentally-observed macroscopic equilibrium behavior.

Dissociation reactions proceed as indicated by the general equation

$$AB + X \rightarrow A + B + X \qquad (1)$$

where $AB$ is diatomic, $A$ and $B$ are monatomic, and $X$ is a partner of any type. Dissociation is possible only for those collisions with energy exceeding the dissociation threshold, $E_d$. This represents the reaction energy which is removed from the energy modes contributing to the reaction and stored in the electron configuration of the products.

Exchange reactions are typically of the form

$$AB + C \rightarrow AC + B \qquad (2)$$

where $C$ is monatomic. Again, collisions must have energy exceeding the threshold, $E_d$, to initiate the reaction. Associated with reaction (2) is its reverse reaction which itself has a threshold energy, $E_{d_{rev}}$. During reaction the energy, $\Delta E_d = E_d - E_{d_{rev}}$, is removed from the energy modes of the reactants and stored as potential energy in the products.

Recombination, the reverse of dissociation, is a three-body process. Benson and Fueno[8] suggest that

recombination should be modeled as a succession of binary collisions. In the first step, given by

$$A + B \rightarrow (AB), \tag{3}$$

two atoms collide and possibly form a mutually orbiting pair, denoted in parentheses as $(AB)$. The pair remains intact for some limited lifetime depending upon the collision energy. If the orbiting pair experiences a collision during that lifetime, then it may stabilize into a molecule, completing the second step of recombination, given by

$$(AB) + X \rightarrow AB + X. \tag{4}$$

Upon stabilization, the reaction energy, $E_d$, from (1) is removed from the electron configuration of the reactants and repartitioned among the energy modes of the products.

If no stabilizing collision occurs, the orbital pair splits into free atoms, representing a standard monatomic thermal collision. Such a 2-step method has been adapted for this simulation as described below.

## SIMULATION FUNDAMENTALS

The pipelining architecture of a vector processing machine, such as the Cray Y-MP, permits simultaneous operations involving collections of data, yielding extremely fast computational throughput. However, algorithms must be structured accordingly in order to utilize this capability. Algorithms which involve complex conditional branching or dependence upon other elements within a single vector are not able to take advantage of this architecture effectively, and suffer a loss in computational throughput[9]. When processing a list of data, the current Stanford simulation handles conditional branches by generating new subset lists for later processing[3]. The positions, velocities, and internal energies of each particle is stored in the *particle array* in computer memory.

The basic steps in a particle simulation are the collisionless motion of particles, followed by the pairing and testing of neighboring particles for possible collision. The collision selection rule is taken from Baganoff and McDonald[2-4], and is based on the power law intermolecular potential. Each class of interaction, involving species $a$ and $b$, has associated with it a unique power-law exponent, $\alpha_{ab}$, and cross-section constant, $\sigma_{ab}$, as used in the collision probability of the form

$$P_c(g_{ab}) \sim \sigma_{ab} g_{ab}^{1-4/\alpha_{ab}} \tag{5}$$

where $g_{ab}$ is the relative speed of collision. The power-law exponent typically ranges from the Maxwell-molecule limit, $\alpha_{ab} = 4$, to the hard-sphere limit, where $\alpha_{ab} = \infty$. The constant, $\sigma_{ab}$, is found by matching some specified reference mean-free-path[4].

Particles in the flow are paired off as potential collision candidates, and $P_c$ is computed per pair from (5). To select colliding pairs from among all candidates, a uniformly generated random number, $\Re$, is compared to that probability such that the collision is accepted if $\Re < P_c$. Those pairs chosen to collide are placed in a new list which is later processed according to the collision mechanics of the method.

An algorithm which models chemistry, compatible with this list generation structure, must interrupt the above procedure as shown in figure 1. After pairs have been selected for collision, they must be tested for reaction. Depending upon the class of collision, distinguished by the types of species involved, colliding pairs are divided into respective class lists. Ideally each class should then be tested for several possible reaction types associated with it. This again involves computation of probability functions as discussed below.

Since testing all possible reactions is expensive for a given colliding pair, a simplification is employed in this simulation which significantly reduces the amount of conditional branching required. That is, ***only one type of reaction is considered per colliding pair.*** This simplification is appropriate given that particles are randomly paired and the sample size is large. Taking advantage of this, the type of reaction considered for the pair is determined not only by the types of particles involved, but also by the specific order in which they appear in the pair, as indicated below:

| | |
|---|---|
| Dissociation 1 | $AB + CD \rightarrow A + B + CD$ |
| Dissociation 2 | $AB + C \rightarrow A + B + C$ |
| Exchange | $C + AB \rightarrow AC + B$ |
| Form Orbital Pair | $A + B \rightarrow (AB)$ |
| Stabilize Orbital Pair | $(AB) + X \rightarrow AB + X$ |

After reactive collisions have been selected, they are processed according to the reaction mechanics models appropriate for the given reaction-type. Collisions which do not react are processed according to standard collision mechanics which may include *thermal* relaxation involving possible energy exchange among the relative translational, rotational, and vibrational modes. Such collision mechanics are discussed in detail by McDonald[4] and reviewed briefly below.

## THERMAL-COLLISION MECHANICS

A collision between particles $a$ and $b$ has associated with it a center of mass velocity, $\mathbf{G}_{ab}$, and relative translational velocity, $\mathbf{g}_{ab} = \mathbf{u}_a - \mathbf{u}_b$. The relative translational energy, $\epsilon_{rel_{ab}}$, is then defined by

$$\epsilon_{rel_{ab}} = \frac{1}{2}\mu_{ab} g_{ab}^2 \tag{6}$$

where $\mu_{ab} = m_a m_b/(m_a + m_b)$ is the reduced mass of the pair. Neglecting the electronic modes, the ener-

gies available in a given collision include $\epsilon_{rel_{ab}}$ and the rotational and vibrational internal energies of $a$ and $b$.

## Mechanics of Elastic Collisions

After an elastic collision, the particles separate with relative translational velocity, $\mathbf{g}'_{ab}$, which is simply a random re-orientation of the collision approach velocity, $\mathbf{g}_{ab}$. This represents spherically uniform scattering of post-collision velocities adapted from the Variable Hard-Sphere (VHS) model of Bird[10]. There is no alteration of the internal modes of either particle. Note the use of superscript $'$ to denote post-collision quantities.

## Mechanics of Rotational Relaxation

Some collisions may permit energy exchange between the translational mode and one or both of the internal energy modes, promoting relaxation of the gas toward thermal equilibrium. Those collisions involving the rotational mode are generally more frequent than those involving vibration.

Rotationally-relaxing thermal collisions involve repartitioning of total energy, $\epsilon_{rel} + \epsilon_{rot}$, among the relative translational and rotational modes of the collision. This is adapted from the method of Borgnakke and Larsen[11] by sampling the fraction,

$$F = \frac{\epsilon_{rot}}{\epsilon_{rel} + \epsilon_{rot}} \tag{7}$$

directly from the equilibrium *distribution*, $f(F)$. Knowing the types of particles involved in the collision, $f(F)$ is easily found and is invariant with temperature when assuming that the translational and rotational energy distributions are continuous. The post-collision rotational energy is then given by

$$\epsilon'_{rot} = (\epsilon_{rel} + \epsilon_{rot})\ F. \tag{8}$$

If both particles in the collision are diatomic, then $\epsilon'_{rot}$ is randomly divided between their respective rotational modes. A probability, $P_{rot}$, is used to select which collisions will include rotational relaxation.

## Mechanics of Vibrational Relaxation

A probability, $P_{vib}$, is used to select which collisions will include vibrational relaxation. These collisions are modeled by McDonald[4] in a manner which avoids direct sampling from equilibrium distributions such as $f(F)$ since they are temperature-dependent when vibrational energy is involved. That model will be adapted here to facilitate its use in reaction mechanics, and is based on an efficient iteration scheme. First, energy is exchanged between rotation and vibration, followed by an exchange between rotation and translation via rotational-relaxation as outlined above. These steps may then be repeated, iterating toward equilibrium.

Note that consideration must be made of the quantum nature of the vibrational mode. For the simple harmonic oscillator we define vibrational energy, measured relative to the ground state, $\frac{1}{2}k\theta_v$, by

$$\epsilon_{vib} = q_{vib}(k\theta_v) \tag{9}$$

where $q_{vib}$ represents the number of quanta associated with a given vibrator, and $k\theta_v$ represents the characteristic vibrational energy per quantum level.

To model the random mixing of rotational and vibrational energies in a manner which promotes equilibrium, we take advantage of the fundamental physical assumption of statistical mechanics[7]. This states that all possible divisions of internal energy,

$$\epsilon_{int} = \epsilon_{rot} + \epsilon_{vib}, \tag{10}$$

among the internal modes, $\epsilon'_{rot}$ and $\epsilon'_{vib}$, are *a priori equally probable*.

First, $\epsilon_{int}$ is quantized by the characteristic vibrational energy, $k\theta_v$, resulting in $Q+1$ quantum levels: 0, 1, ... $Q$. The limit, $Q$, is found from

$$Q = \left\lfloor \frac{\epsilon_{int}}{k\theta_v} \right\rfloor, \tag{11}$$

where the brackets, "$\lfloor\ \rfloor$", denote truncation.

Upon division, the outcome quantum level for vibration, $q'_{vib}$, must be equally likely among these $Q+1$ quantum levels. A means of doing this is simply to generate a floating-point random number in the range $[0, Q+1]$, and truncate to the nearest level, as given by

$$q'_{vib} = \left\lfloor \Re(Q+1) \right\rfloor \tag{12}$$

where $\Re$ is a uniformly generated random number in the range $[0, 1]$. From (12), the new vibrational energy given by

$$\epsilon'_{vib} = q'_{vib}(k\theta_v). \tag{13}$$

The remaining internal energy is placed in the rotational mode according to

$$\epsilon'_{rot} = \epsilon_{int} - \epsilon'_{vib}. \tag{14}$$

As proven in the Appendix, applying this method of energy partition among the internal modes of a diatomic molecule will satisfy detailed balance between the vibrational and rotational modes at equilibrium. However, when out of equilibrium, the additional rotational-relaxation steps are required to promote equilibrium distributions.

# ENERGY MODES IN REACTION

For dissociation reaction (1), only collisions with total energy exceeding the activation energy, $E_d$, are capable of dissociating molecule $AB$. That total collision energy, $\epsilon_c = \Sigma\epsilon_m$, is the sum of energy from all contributing modes, $m$, and is distributed in a Boltzmann

distribution with $\zeta_c$ fractional degrees of freedom[12], given by

$$f_c(\epsilon_c)d\epsilon_c = \frac{1}{\Gamma(\zeta_c/2)}\left(\frac{\epsilon_c}{kT}\right)^{\zeta_c/2-1} e^{-\epsilon_c/kT}\frac{d\epsilon_c}{kT}. \quad (15)$$

There has been considerable debate, however, regarding the role of internal energy modes in dissociation[13]. It has been unclear which of the energy modes, available in a given collision, contribute to $\epsilon_c$, leading to confusion over the appropriate value of $\zeta_c$. Various theories on chemical kinetics suggest that reactions occur as a result of intimate interactions among the internal energy modes of the reactants. Sharma, Huo, and Park[14] suggest that dissociation is the result of vibration-vibration energy exchange between molecules. Here, $AB$ acquires vibrational energy from partner $X$ until it reaches its reaction threshold and dissociates. Hansen[15] suggests that the rotational modes contribute to vibrational excitation and possible dissociation. Such arguments imply that all modes contribute, in some way, to $\epsilon_c$. In addition, since only those collisions for which $\epsilon_c > E_d$ are dissociation candidates, it is advantageous to include all available energy modes in the $\epsilon_c$ sum, resulting in a greater number of sufficiently energetic collisions, and thus increasing the sample size for reaction selection.

This debate concerning internal energy mode contribution to reaction may be partly resolved in a self-consistent manner by consideration of detailed balance as derived by Haas[16]. More involved reaction selection models, fully coupling internal modes to dissociation, have been studied extensively[14,17] but have yet to appear in large-scale particle simulations.

Including all available energy modes in the collision energy,

$$\epsilon_c = \epsilon_{rel_{AB,X}} + \epsilon_{int_{AB}} + \epsilon_{int_X}, \quad (16)$$

the degrees of freedom for $f_c(\epsilon_c)$ is simply the sum of degrees of freedom from each of these statistically independent modes[16],

$$\zeta_c = \left(4 - \frac{4}{\alpha_{AB,X}}\right)_{rel} + \zeta_{int_{AB}} + \zeta_{int_X}, \quad (17)$$

where the subscripts denote the energy modes contributing to $\zeta_c$. In (17) the $4 - 4/\alpha_{AB,X}$ term accounts for the relative translational energy biased by the collision selection rule (5). Due to the rotational and vibrational internal energies, the internal degrees of freedom of $AB$ is

$$\zeta_{int_{AB}} = 2 + \zeta_{vib_{AB}}. \quad (18)$$

Similarly, $\zeta_{int_X}$ is zero if $X$ is monatomic, and is given by (18) if diatomic. Normally, the vibrational mode at equilibrium has associated with it $\zeta_{vib}$ degrees of freedom, defined for the simple harmonic oscillator by[7]

$$\zeta_{vib} = \frac{2\theta_v/T}{e^{\theta_v/T} - 1}. \quad (19)$$

Given that all available energy modes contribute to the reaction, in simulating the chemistry, all modes must be used in the reaction selection rules, and all must be affected by the reaction mechanics, as presented below.

## DISSOCIATION SELECTION

Chemistry modeling involves determining which collisions react (reaction selection) and then performing the reactions (reaction mechanics). The probability, $P_d$, that a given collision between particles $AB$ and $X$ results in dissociation of $AB$ as in (1) is computed as a function of the energies contributing to the collision. A uniformly generated random number, $\Re$, is compared to that probability such that dissociation is accepted if $\Re < P_d$.

The expression for $P_d$ must be determined such that the resultant forward reaction rates at equilibrium match those from experiment. Possible forms of this function have been suggested[15] based upon the physics of the chemical interaction kinetics and are adapted here in the format given by Bird[18], as

$$P_d(\epsilon_c) = \beta_d \frac{(\epsilon_c - E_d)^{\psi + \frac{\zeta_c}{2} - 1}}{(\epsilon_c)^{\frac{\zeta_c}{2} - 1}}. \quad (20)$$

By matching the temperature dependence of the simulated dissociation rate due to application of (20), against the the Arrhenius fit[19] for the rate coefficient from experiment, given by

$$k_f(T) = a_f T^{b_f} e^{-E_d/kT} \quad (21)$$

the free parameters in $P_d(\epsilon_c)$ are found to be[16]

$$\psi = b_f - \frac{1}{2}\left(1 - \frac{4}{\alpha_{AB,X}}\right) \quad (22)$$

and

$$\beta_d = \frac{a_f \sqrt{\frac{\pi}{4}} \left(\frac{\mu}{2k}\right)^{\frac{1}{2} - \frac{2}{\alpha_{AB,X}}} \Gamma(\zeta_c/2)}{\sigma_{AB,X}\, \Gamma\left(2 - \frac{2}{\alpha_{AB,X}}\right) \Gamma\left(\frac{\zeta_c + 2\psi}{2}\right) k^{\psi}}. \quad (23)$$

Note that $\mu = \mu_{AB,X}$ is the reduced mass, $k$ is Boltzmann's constant, and $a_f$ and $b_f$ are unique constants per reaction.

With the exception of $\zeta_c$, all parameters in $P_d(\epsilon_c)$ are constant. However, $\zeta_{vib}$ and thus $\zeta_{int}$ and $\zeta_c$ are very *weak* functions of temperature for the range of interest in hypersonic flow, as shown in figure 2. We therefore fix $\zeta_{vib}$ at some reference temperature, $T_{ref}$, for use in $P_d$. An appropriate $T_{ref}$ is any intermediate translational temperature taken from that portion of the flowfield dominated by reactions. Figure 3 shows

the form of $f_c(\epsilon_c)$ at several temperatures along with an example of $P_d(\epsilon_c)$.

Exchange reactions are also selected via $P_d$ with the exception that $\zeta_{int_X}$ is zero.

## RECOMBINATION SELECTION

As noted earlier, recombination is modeled by a 2-step process. All collisions between atoms result in the formation of orbital pairs as given by (3). Even for a highly dissociated flowfield, the concentration of $(AB)$ remains very low. During the next timestep, all $(AB)$ which collide with partner $X$ are tested for stabilization by the recombination probability function

$$P_r(\epsilon_{int_o}, \epsilon_{int_X}) = \beta_r (\epsilon_{int_o})^{-\phi_o} (\epsilon_{int_X})^{-\phi_x} \qquad (24)$$

where $\epsilon_{int_o}$ and $\epsilon_{int_X}$ are the internal energies of the orbital pair $(AB)$ and partner $X$, and $\beta_r$, $\phi_o$, and $\phi_x$ are unique constants per reaction. For monatomic X, $\epsilon_{int_X}$ is excluded from (24). Note the use of subscript "$o$" to denote orbital pairs, $(AB)$. Those collisions selected (by comparison of a random number, $\Re$, to $P_r$), will complete the recombination process of equation (4).

The form of $P_r$ in (24) was chosen because it leads to the correct temperature dependence of the equilibrium concentration coefficient, $K$, defined for reaction (1) by

$$K = \frac{n_A n_B}{n_{AB}} \qquad (25)$$

where $K(T)$ typically assumes an Arrhenius temperature fit from experiment,

$$K(T) = a_e T^{b_e} e^{-E_d/kT}. \qquad (26)$$

The parameters in $P_r$, as well as the unknown interaction potential for the collisions involving orbital pairs, $\alpha_{(AB),X}$, are found in a manner similar to that employed for dissociation. However, a complete derivation involves consideration of detailed balance among the energy modes contributing to the reaction, and is given by Haas[16]. From that derivation, the recombination parameters are found to be

$$\alpha_{(AB),X} = \frac{4}{4/\alpha_{AB,X} - 2\psi \frac{4-4/\alpha_{AB,X}}{\zeta_c}} \qquad (27)$$

$$\phi_o = 2 - \frac{2}{\alpha_{A,B}} - \frac{\zeta_{int_{AB}}}{2} - \psi \frac{\zeta_{int_{AB}}}{\zeta_c} \qquad (28)$$

$$\phi_x = -\psi \frac{\zeta_{int_X}}{\zeta_c} \qquad (29)$$

and

$$\beta_r = \frac{\pi (1+\delta_{A,B})\, \Delta t\, (a_f/a_e)}{2^{3-\frac{2}{\alpha_3}-\frac{2}{\alpha_4}}\, k^{b_f-b_e}} \frac{\mu_3^{\frac{1}{2}-\frac{2}{\alpha_3}}\, \mu_4^{\frac{1}{2}-\frac{2}{\alpha_4}}}{\sigma_3\, \sigma_4} \frac{\Gamma(\frac{\zeta_{int_X}}{2})}{\Gamma(2-\frac{2}{\alpha_4})\Gamma(2-\frac{2}{\alpha_3}-\phi_o)\Gamma(\frac{\zeta_{int_X}}{2}-\phi_x)} \qquad (30)$$

where subscripts 3 and 4 correspond to the reactions as given by equations (3) and (4), respectively, $\Delta t$ is the duration of the timestep, $\delta_{A,B}$ is the Kronecker delta, and $\psi$ is given by (22).

These reaction selection rules are functions of collision energies, and should therefore be applicable throughout the flowfield. The free parameters of these functions were determined from known equilibrium experimental data.

## REACTION MECHANICS

Once reactive collisions have been identified via reaction selection rules (20) and (24), the mechanics of those reactions must be performed.All reactions of interest in hypersonics involve some alteration of the energy modes contributing to the reaction. The objective here is to determine how to remove or add energy to each of the energy modes involved in the reaction just prior to splitting or forming particles into products. The chemical-kinetic details are not well understood regarding energy partition among the energy modes of particles during reaction. However, the modeling of reaction mechanics must adhere to certain fundamental constraints, including detailed balance at equilibrium, and conservation of momentum and energy.

### Proportional Energy-Exchange Model

Recall the energies contributing to dissociative collision (1) as identified by (16). The dissociation energy must be removed from the collision energy,

$$\epsilon_c'' = \epsilon_c - E_d \qquad (31)$$

$$= \epsilon_{rel_{AB,X}} + \epsilon_{rot_{AB}} + \epsilon_{vib_{AB}} + \epsilon_{int_X} - E_d \qquad (32)$$

$$= \epsilon''_{rel_{AB,X}} + \epsilon''_{rot_{AB}} + \epsilon''_{vib_{AB}} + \epsilon''_{int_X}. \qquad (33)$$

Note the use of superscript $''$ to denote post-reaction quantities.

Though it is unclear how to redistribute the energies of (32) among those of (33), a convenient means by which to account for the alteration of each energy mode, $m$, is to *proportionally* remove the reaction energy, $E_d$, resulting in post-dissociation mode energies, $\epsilon_m''$, given by

$$\epsilon_m'' = \epsilon_m - \frac{\epsilon_m}{\epsilon_c} E_d = \epsilon_m \left(1 - \frac{E_d}{\epsilon_c}\right). \qquad (34)$$

This method is simple to implement and can be applied to exchange reactions and recombination as well. Note, however, that in exothermic reactions, $E_d$ will be proportionally added to each contributing energy mode rather than removed.

At equilibrium, detailed balance dictates that there exists no net energy transfer among energy modes of all species in the gas[7]. As a consequence, the reaction

models must promote, or relax to, equilibrium for a gas in thermochemical non-equilibrium. If a relaxing ensemble of particles reaches steady-state, yet exhibits non-equilibrium behavior such as a difference in mode temperatures, then the reaction model is in error.

Just as in the method of Borgnakke and Larsen[11], partitioning post-reaction energies by sampling directly from equilibrium distributions would naturally accomplish this. However, that requires that these distributions be available at all temperatures for all possible reactions. Alternatively, the proportional energy-exchange model above avoids this difficulty since it requires no access to equilibrium distributions, but falters in that it will not readily promote equilibrium for a flow initially in thermal non-equilibrium. It is therefore necessary to add thermally-relaxing steps, as in (7)-(14), to this algorithm for reaction mechanics.

## Mechanics of Dissociation

Dissociation reaction (1) is divided into two steps. First, the dissociation energy is removed from the reactants, creating temporary products, as described by

$$AB + X \longrightarrow AB'' + X''. \tag{35}$$

The products, $AB''$ and $X''$, separate with relative translational energy, $\epsilon''_{rel_{AB,X}}$, modified according to the proportional energy-exchange model of (34). As mentioned earlier, decomposing a relative energy into post-collision velocities involves random re-orientation of the post-reaction relative velocity vector, $\mathbf{g}''_{AB,X}$, as found from $\epsilon''_{rel_{AB,X}}$ and equation (6).

If $X$ is diatomic, the post-dissociation states of its internal energies are not found individually by application of (34), since consideration must be made of the quantum nature of the vibrational mode. Rather, the internal energy as a whole is depleted according to (34),

$$\epsilon''_{int_X} = \epsilon_{int_X}\left(1 - \frac{E_d}{\epsilon_c}\right) \tag{36}$$

and is then redistributed between $\epsilon''_{rot_X}$ and $\epsilon''_{vib_X}$ according to the steps employed for vibrational relaxation in equations (11)-(14). If $X$ is monatomic, $\epsilon_{int_X}$ will remain zero.

Now that $AB''$ and $X''$ have separated, the second step in the dissociation reaction involves splitting $AB''$ into free atoms, given by

$$AB'' \longrightarrow A + B. \tag{37}$$

In order to conserve linear momentum and energy, all of the post-dissociation internal energy of $AB''$ must go into the relative translational energy for the separation of $A$ and $B$. That is,

$$\epsilon_{rel_{A,B}} = \epsilon''_{int_{AB}} = (\epsilon_{rot_{AB}} + \epsilon_{vib_{AB}})\left(1 - \frac{E_d}{\epsilon_c}\right). \tag{38}$$

The mechanics for exchange reactions (2) are similar to that for dissociation, replacing $E_d$ by $\Delta E_d = E_d - E_{d_{rev}}$.

## Mechanics of Orbital Pair Formation

Orbital pair formation is the first step in recombination modeling as given by (3), where two atoms, $A$ and $B$, join to form a single temporary orbital pair, $(AB)$. Conservation of linear momentum dictates that the velocity of $(AB)$ must be the same as the center of mass velocity of the $A + B$ collision, $\mathbf{G}_{A,B}$. Conservation of energy requires that the relative translational energy, $\epsilon_{rel_{A,B}}$, must be stored internally in $(AB)$,

$$\epsilon_{int_{(AB)}} = \epsilon_{rel_{A,B}}. \tag{39}$$

If $(AB)$ remains uncollided on the next time step, it is split into free atoms $A$ and $B$. Doing so simply requires that $\epsilon_{int_{(AB)}}$ be converted back into $\epsilon_{rel_{A,B}}$.

## Mechanics of Orbital Pair Stabilization

Orbital pair stabilization, given by (4), represents the second step which completes the recombination reaction. The reaction energy, $E_d$, must be absorbed by the energy modes of the products, such that the post-reaction collision energy is given by

$$\begin{aligned} \epsilon''_c &= \epsilon_{rel_{(AB),X}} + \epsilon_{int_{(AB)}} + \epsilon_{int_X} + E_d \\ &= \epsilon''_{rel_{(AB),X}} + \epsilon''_{int_{(AB)}} + \epsilon''_{int_X} \\ &= \epsilon_{rel_{AB,X}} + \epsilon_{int_{AB}} + \epsilon''_{int_X} \end{aligned} \tag{40}$$

According to the proportional energy-exchange concept, the relative translational energy of separation of stabilized molecule $AB$ and collision partner $X$ is found by adapting (34),

$$\epsilon_{rel_{AB,X}} = \epsilon''_{rel_{(AB),X}} = \epsilon_{rel_{(AB),X}}\left(1 + \frac{E_d}{\epsilon_c}\right). \tag{41}$$

The internal energies of $X$, if applicable, are found in the same way as in dissociation from equation (36), with the exception that reaction energy is added rather than removed.

Likewise, the internal energy of $AB$, given by

$$\epsilon_{int_{AB}} = \epsilon''_{int_{(AB)}} = \epsilon_{int_{(AB)}}\left(1 + \frac{E_d}{\epsilon_c}\right) \tag{42}$$

is distributed among its rotational and vibrational modes according to the method employed for vibrational relaxation in equations (11)-(14). However, as stated earlier and as proven in the appendix, these steps must be augmented by rotational relaxation to promote equilibrium distributions for flow initially out of equilibrium.

## RESERVOIR SIMULATION

A single-species, adiabatic reservoir of molecules, superheated in translation and rotation only, will relax to thermochemical equilibrium through reactions and energy-mode exchanges. The final temperature, $T^*$, and composition can be determined analytically[20]. The relaxation history of this reservoir is similar to that behind a normal shock wave.

In the external flows typically associated with hypersonic re-entry vehicles, dissociation and exchange reactions dominate the flowfield chemistry[17]. However, the objective here is to test the simulation in an environment in which *all* types of chemical reactions (dissociation, exchange, and recombination) are pronounced, such as would occur at equilibrium if the temperature and diatomic concentrations remained high. Consequently, to simulate thermochemical relaxation to equilibrium, a model species, $A_2$, is used which is similar to $O_2$ except that $a_e = 0.10$ rather than 1200 as given in table 1. This effectively increases the recombination rate, allowing greater concentration of diatomic particles at high equilibrium temperature where reactions are significant. Such a gas represents a "worst-case scenario" in which recombination has pronounced effects to better demonstrate the capability of the reaction models. The reactions pertaining to $A_2$ are

$$A_2 + A_2 \rightleftharpoons A + A + A_2 \tag{43}$$

$$A_2 + A \rightleftharpoons A + A + A. \tag{44}$$

As plotted in figure 4, $A_2$ was relaxed from 16,871K to steady state. The mode temperatures corresponding to translation, rotation, and vibration are plotted in time, and converge to the equilibrium temperature, analytically determined to be $T^* = 7,000$K. The rates of internal mode relaxation were controlled by invariant inelastic collision probabilities, $P_{rot} = 0.20$ and $P_{vib} = 0.02$, adapted from Bird[20]. Energy-dependent forms of these probabilities, suggested by Boyd[17], would better model thermal relaxation in the transient portion of the flow, but are of little benefit here in studying equilibrium behavior. The simulation started with 40,000 diatomic particles and ran for 1500 transient steps and 1000 steady-state sampling steps.

The relaxation simulation was then repeated for temperatures in the range 5,000K< $T^*$ <15,000K, with reference temperature $T_{ref} = 10,000$K. For each case, the resulting equilibrium temperature per mode reached by the simulation is compared to the analytic value in figure 5. The close agreement between mode temperatures indicates that detailed balance is maintained, as is necessary for equilibrium. The simulated forward rate coefficient per reaction is plotted against $T^*$ in figure 6, and is compared to the experimental curve of $k_f(T^*)$. Likewise, figure 7 compares the degree of dissociation, $\Delta_d$, for these runs against the experimental fit, where[7]

$$\Delta_d = \frac{n_A}{2n_{A_2} + n_A} \tag{45}$$

and

$$K = 2(2n_{A_2} + n_A)\frac{\Delta_d^2}{1 - \Delta_d}. \tag{46}$$

These plots indicate that the simulation does capture the correct equilibrium behavior of a relaxing gas as predicted by the experimental fits of the reaction rates and species concentrations over a large temperature range.

The simulation was then run for the 5-species mixture to demonstrate its applicability to hypersonic air chemistry. The gas, composed of 79% $N_2$ and 21% $O_2$, is superheated in translation and rotation to 15,000K, and allowed to relax thermochemically toward equilibrium. The plot of species concentration relaxation is given by figure 8. Note the rapid increase in the concentration of atomic oxygen as $O_2$ quickly dissociates. Likewise, dissociation of $N_2$ results in production of nitrogen atoms, followed eventually by formation of $NO$ via recombination and exchange reactions.

## CONCLUDING REMARKS

The chemistry algorithms presented here are compatible with the existing vectorized simulation of Baganoff and McDonald[2-5]. The dissociation selection models adequately yield the correct forward reaction rates of chemical reactions in a test gas as found experimentally near equilibrium. The recombination selection models also yield correct reaction rate behavior as indicated by the close agreement with experimental fits of equilibrium species concentrations and the resultant steady-state temperature. The reaction mechanics models, based on proportional energy-exchange, conveniently account for the effects of reaction on participating particles in a manner consistent with the constraints of detailed balance and conservation of linear momentum and energy. However, essential to these routines is the inclusion of thermal-relaxation steps which promote thermal equilibrium.

No direct attempt was made here to model the transient of the relaxing bath; comparisons to known behavior were only made at equilibrium. However, the chemistry models are based on molecular interaction physics, independent of the equilibrium assumption which is used only to evaluate unknown parameters. Keeping in mind the fundamentals as outlined here, one can devise more sophisticated chemistry models, possibly involving more species and greater coupling of internal modes to reaction, which adequately simulates the thermochemical phenomena of interest.

## APPENDIX
### Proof of Equilibrium Convergence

The algorithm described by equations (11)-(14) for re-distributing internal energy represents random mixing of continuous and discrete distributions pertaining to the rotational and vibrational energy modes, respectively. The objective here is to prove that this algorithm promotes equilibrium.

The equilibrium distribution of rotational energy, for which $\zeta_{rot} = 2$, can be rewritten from (15) in the form

$$f^*(\varepsilon) = e^{-\varepsilon} d\varepsilon, \tag{47}$$

where $\varepsilon = \epsilon_{rot}/kT$ is normalized energy, and superscript * denotes equilibrium. Quantizing this distribution with respect to the normalized characteristic energy of vibration, $\bar{\varepsilon} = k\theta_v/kT$, results in the discrete equilibrium distribution over vibrational quantum levels, $i$,

$$\begin{aligned} P^*(i) &= \int_{i\bar{\varepsilon}}^{(i+1)\bar{\varepsilon}} f_r^*(\varepsilon) d\varepsilon \\ &= \omega^i(1-\omega) \end{aligned} \tag{48}$$

where $\omega = e^{-\bar{\varepsilon}} \leq 1$ is a convenient grouping of terms. For a given rotational energy, $\varepsilon$, we associate a quantum value, $j = \lfloor \varepsilon/\bar{\varepsilon} \rfloor$, which is also distributed as in (48), such that the total quanta from (11) is $Q = i + j$. The normalized surplus energy remaining after truncation is defined by

$$\xi = \varepsilon - j\bar{\varepsilon}, \tag{49}$$

and is distributed according to $f^*(\varepsilon)$ upon renormalizing over the quantum level, $j$, for which $d\xi = d\varepsilon$,

$$\begin{aligned} f_t^*(\xi) d\xi &= \frac{f^*(\varepsilon) d\varepsilon}{\int_{j\bar{\varepsilon}}^{(j+1)\bar{\varepsilon}} f^*(\varepsilon) d\varepsilon} \\ &= \frac{e^{-(j\bar{\varepsilon}+\xi)} d\xi}{e^{-j\bar{\varepsilon}}(1-e^{-\bar{\varepsilon}})} \\ &= \frac{e^{-\xi}}{(1-\omega)}\, d\xi. \end{aligned} \tag{50}$$

Note that $f_t^*(\xi)$ is independent of rotational quantum level, $j$.

Baganoff[21] arrived at the outcome distributions, $P(i')$ and $P(j')$, in the following manner. Let $i'$ and $j'$ denote the outcome quantum levels due to uniform, random division of total quanta, $Q$. The *conditional* distribution for $i'$, given $Q$, is therefore constant over the $Q+1$ possible outcomes,

$$P(i' \mid Q) = \frac{1}{Q+1}. \tag{51}$$

The *joint* distribution of $i'$ and $Q$ is then

$$P(i', Q) = P(i' \mid Q)\; P_Q^*(Q) \tag{52}$$

where the distribution of $Q$ is given by

$$\begin{aligned} P_Q^*(Q) &= P^*(0)P^*(Q) + P^*(1)P^*(Q-1) + \ldots \\ &= \sum_{i=0}^{Q} P^*(i)P^*(Q-i) \end{aligned} \tag{53}$$

The resulting distribution over $i'$ is found by summing (52) over all Q,

$$\begin{aligned} P(i') &= \sum_{Q=i'}^{\infty} \sum_{i=0}^{Q} P^*(i)P^*(Q-i)P(i' \mid Q) \\ &= \sum_{Q=i'}^{\infty} \sum_{i=0}^{Q} \frac{(1-\omega)^2\omega^Q}{Q+1} \\ &= (1-\omega)^2 \sum_{Q=i'}^{\infty} \omega^Q \\ &= (1-\omega)^2\omega^{i'} \sum_{k=0}^{\infty} \omega^k \\ &= \omega^{i'}(1-\omega) \end{aligned} \tag{54}$$

Comparison of (54) to (48) proves that the algorithm maintains the *discrete* equilibrium distributions for vibration and rotation.

The rotational energy after mixing is

$$\epsilon' = j'\bar{\varepsilon} + \xi \tag{55}$$

where $j' = Q - i'$, such that $d\epsilon' = d\xi$ over the quantum interval, $j'$. The conditional distribution of outcomes for $\epsilon'$ is simply the joint distribution of $j'$ and $\xi$, given $Q$, found by multiplying (51) and (50),

$$\begin{aligned} f(\epsilon' \mid Q) d\epsilon' &= P(j' \mid Q) f_t^*(\xi) d\xi \\ &= \frac{e^{-\xi} d\xi}{(Q+1)(1-\omega)}. \end{aligned} \tag{56}$$

Following the same development as in (54), we solve for the distribution over $\epsilon'$ by summing the joint distribution over all $Q$,

$$\begin{aligned} f(\epsilon') d\epsilon' &= \sum_{Q=j'}^{\infty} \sum_{j=0}^{Q} P^*(j)P^*(Q-j) f(\epsilon' \mid Q) d\epsilon' \\ &= \sum_{Q=j'}^{\infty} \sum_{j=0}^{Q} \frac{(1-\omega)\,\omega^Q\, e^{-\xi}\, d\xi}{Q+1} \\ &= (1-\omega)\, e^{-\xi}\, d\xi \sum_{Q=j'}^{\infty} \omega^Q \\ &= (1-\omega)\, e^{-\xi}\, \omega^{j'}\, d\xi \sum_{k=0}^{\infty} \omega^k \\ &= (1-\omega) e^{-\xi} e^{-j'\bar{\varepsilon}} \frac{1}{(1-\omega)} d\xi \\ &= e^{-(j'\bar{\varepsilon}+\xi)} d\xi \\ &= e^{-\epsilon'} d\epsilon' \end{aligned} \tag{57}$$

Equations (54) and (57) prove that the mixing algorithm maintains both the discrete and continuous distributions at equilibrium.

Note that (53) represents a convolution of the discrete distributions, $P(i)$ and $P(j)$. By virtue of the central limit theorm, repeated convolution and division by $Q + 1$ will result in relaxation of these distributions toward equilibrium if they are initially out of equilibrium. However, the continuous distribution, $f(\epsilon')$, will only reach equilibrium if both $P(j')$ and $f_\epsilon(\xi)$ equilibrate. Unfortunately, the distribution over $\xi$ experiences no convolution in this algorithm, and therefore will not relax toward equilibrium unless additional rotational relaxation steps are included.

To test the algorithm, a reservoir was initialized with no vibrational energy and with rotational energy uniformly distributed, and was then thermally relaxed via the mixing algorithm described here. Two testcases were run, onc which included the rotational relaxation steps, and one which did not. The initial and final distributions for rotation are shown in figure 9, along with the final distribution for vibration. Note that both the discrete and the continuous distributions are Boltzmann for the algorithm which included rotational relaxation. However, when rotational relaxation was excluded, the continuous distribution within each quantum interval did not relax, but remained uniformly distributed. These tests prove that, for a gas out of equilibrium, the mixing algorithm will relax the discrete distributions to equilibrium, but additional rotational-relaxation is needed to achieve equilibrium for the continuous distribution.

## ACKNOWLEDGEMENTS

The author acknowledges and appreciates the guidance of Prof. D. Baganoff and the assistance of Drs. J. D. McDonald, W. Feiereisen, and I. Boyd. Also acknowledged is the support of NASA-Ames for use of their facilities. This work is sponsored by Air Force Office of Scientific Research Grant No. AFOSR 88-0139, and NASA Grant No. NAGW-965.

## REFERENCES

[1] Celenligil, M., Bird, G.A., and Moss, J.N., "Direct Simulation of Three-Dimensional Hypersonic flow About Intersecting Blunt Wedges," AIAA Paper No. 88-0463 (1988)

[2] Baganoff, D. and McDonald, J.D.,"A Collision-Selection Rule for a Particle Simulation Method Suited to Vector Computers," Submitted to *Physics of Fluids* (1990)

[3] McDonald, J.D., and Baganoff, D., "Vectorization of a Particle Simulation Method for Hypersonic Rarefied Flow," AIAA Paper No. 88-2735 (1988)

[4] McDonald, J.D., "A Computationally Efficient Particle Simulation Method Suited to Vector Computer Architectures," Ph.D. Thesis, Department of Aeronautics and Astronautics, Stanford University, December 1989

[5] Feiereisen, W.J., and McDonald, J.D., "Three Dimensional Discrete Particle Simulation of an AOTV," AIAA Paper No. 89-1711 (1989)

[6] Moss, J.N., and Bird, G.A.,"Direct Simulation of Transitional Flow for Hypersonic Reentry Conditions," *Progress in Aeronautics and Astronautics*, Vol. 96, pp. 113-139 (1985)

[7] Vincenti, W.G. and Kruger, C.H., *Introduction to Physical Gas Dynamics*, Wiley (1965)

[8] Benson, S.W. and Fueno, T.,"Mechanism of Atom Recombination by Consecutive Vibrational Deactivations," *Journal of Chemical Physics*, Volume 16, No. 6, pp. 1597-1607 (1962)

[9] Padua, D.A., and Wolfe, M.J.,"Advanced Compiler Optimization for Supercomputers," *Communications of the ACM*, Volume 29, No. 12, pp. 1184-1201 (1986)

[10] Bird, G.A., "Monte-Carlo Simulation In An Engineering Context," *AIAA Progress in Astronautics and Aeronautics: Rarefied Gas Dynamics*, Vol. 74, Part 1, edited by Sam S. Fisher, pp. 239-255 (1981)

[11] Borgnakke, C. and Larsen, P.S.,"Statistical Collision Model for Monte Carlo Simulation of Polyatomic Gas Mixture," *Journal Of Computational Physics* No. 18, pp. 405-420 (1975)

[12] Hinshelwood, C.N., *The Kinetics of Chemical Change*, Claredon Press, Oxford (1940)

[13] Clarke, J.F., and McChesney, M.,*Dynamics of Relaxing Gases*, Second Edition, Butterworths (1976)

[14] Sharma, S.P., Huo, W.M., and Park, C.,"The Rate Parameters For Coupled Vibration-Dissociation In A Generalised SSH Approximation," AIAA Paper No. 88-2714 (1988)

[15] Hansen, C.F.,"Rate Processes in Gas Phase," *NASA Reference Publication 1090*, May (1983)

[16] Haas, B.L., "Thermochemistry Models Applicable To A Vectorized Particle Simulation," Ph.D. Thesis, Department of Aeronautics and Astronautics, Stanford University, December 1990

[17] Boyd, I.,"Assessment of Chemical Nonequilibrium in Rarefied Hypersonic Flow," AIAA Paper No. 90-0145 (1990)

[18] Bird, G.A., "Simulation of Multi-Dimensional and Chemically Reacting Flows," *Rarefied Gas Dynamics*, ed. by R. Campargue, Volume I, pp.365-388, (1976)

[19] Bortner, M.H.,"A Review of Rate Constants of Selected Reactions of Interest in Re-Entry Flow Fields in the Atmosphere," *NBS Technical Note 484* (1969)

[20] Bird, G.A., "Direct Molecular Simulation of a Dissociating Gas," *Journal of Computational Physics* Volume 25, pp. 353-365 (1977)

[21] Baganoff, D., private communication (1988)

Table 1. Reaction equations and data[6,7,19] for the 5-species air model.

| REACTION | $a_f$ | $b_f$ | $a_e$ | $b_e$ | $E_d/k$ $(K)$ |
|---|---|---|---|---|---|
| $N_2 + N_2 \rightleftharpoons N + N + N_2$ | $6.17 \times 10^{-9}$ | -1.60 | 18 | 0.0 | 113,000 |
| $N_2 + O_2 \rightleftharpoons N + N + O_2$ | $6.17 \times 10^{-9}$ | -1.60 | 18 | 0.0 | 113,000 |
| $N_2 + NO \rightleftharpoons N + N + NO$ | $6.17 \times 10^{-9}$ | -1.60 | 18 | 0.0 | 113,000 |
| $N_2 + N \rightleftharpoons N + N + N$ | $1.85 \times 10^{-8}$ | -1.60 | 18 | 0.0 | 113,000 |
| $N_2 + O \rightleftharpoons N + N + O$ | $1.85 \times 10^{-8}$ | -1.60 | 18 | 0.0 | 113,000 |
| $O_2 + N_2 \rightleftharpoons O + O + N_2$ | $4.58 \times 10^{-11}$ | -1.00 | 1200 | -0.5 | 59,500 |
| $O_2 + O_2 \rightleftharpoons O + O + O_2$ | $4.58 \times 10^{-11}$ | -1.00 | 1200 | -0.5 | 59,500 |
| $O_2 + NO \rightleftharpoons O + O + NO$ | $4.58 \times 10^{-11}$ | -1.00 | 1200 | -0.5 | 59,500 |
| $O_2 + N \rightleftharpoons O + O + N$ | $1.37 \times 10^{-10}$ | -1.00 | 1200 | -0.5 | 59,500 |
| $O_2 + O \rightleftharpoons O + O + O$ | $1.37 \times 10^{-10}$ | -1.00 | 1200 | -0.5 | 59,500 |
| $NO + N_2 \rightleftharpoons N + O + N_2$ | $3.83 \times 10^{-13}$ | -0.50 | 4 | 0.0 | 75,550 |
| $NO + O_2 \rightleftharpoons N + O + O_2$ | $3.83 \times 10^{-13}$ | -0.50 | 4 | 0.0 | 75,550 |
| $NO + NO \rightleftharpoons N + O + NO$ | $3.83 \times 10^{-13}$ | -0.50 | 4 | 0.0 | 75,550 |
| $NO + N \rightleftharpoons N + O + N$ | $7.66 \times 10^{-13}$ | -0.50 | 4 | 0.0 | 75,550 |
| $NO + O \rightleftharpoons N + O + O$ | $7.66 \times 10^{-13}$ | -0.50 | 4 | 0.0 | 75,550 |
| $N_2 + O \rightarrow NO + N$ | $5.30 \times 10^{-17}$ | 0.10 | | | 37,500 |
| $NO + N \rightarrow N_2 + O$ | $2.02 \times 10^{-17}$ | 0.10 | | | 0 |
| $O_2 + N \rightarrow NO + O$ | $5.20 \times 10^{-22}$ | 1.29 | | | 3,600 |
| $NO + O \rightarrow O_2 + N$ | $3.60 \times 10^{-22}$ | 1.29 | | | 19,700 |

Note: $k_f$ from equation (13) is in units of $m^3/(molecule\text{-}s)$, $K$ from equation (18) is in units of $mole/cm^3$, and $T$ is in Kelvin.

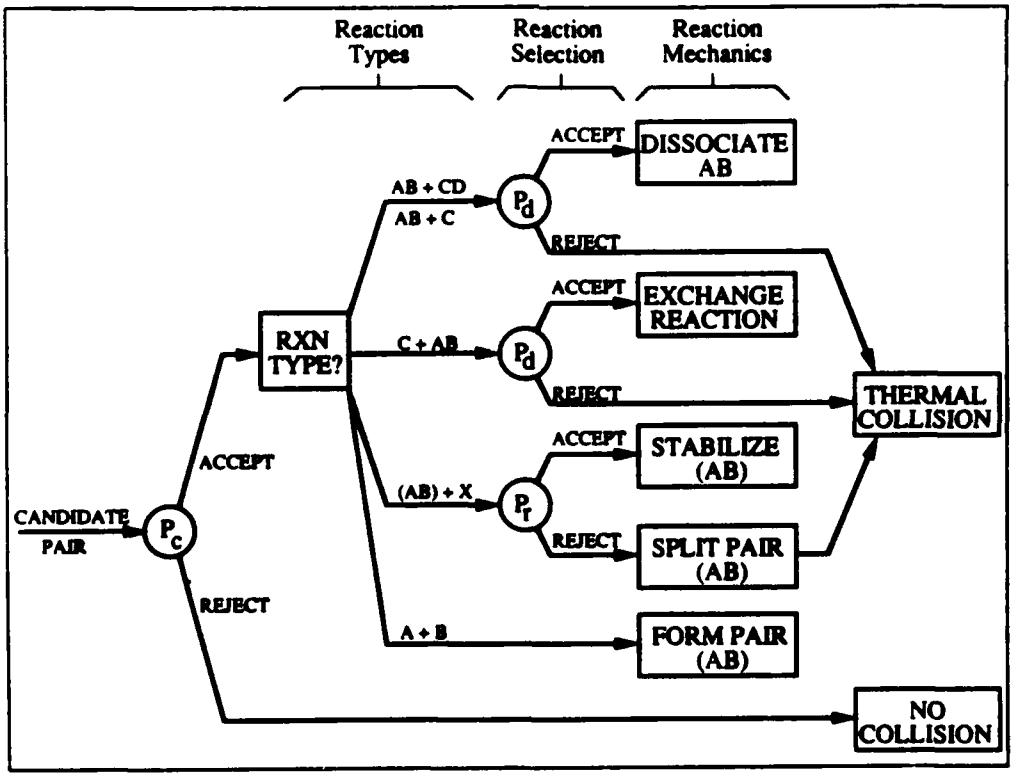


Fig. 1. Adaptation of a vector-compatible collision algorithm to include chemistry. Reaction-type identification, reaction-selection, and reaction-mechanics are added.

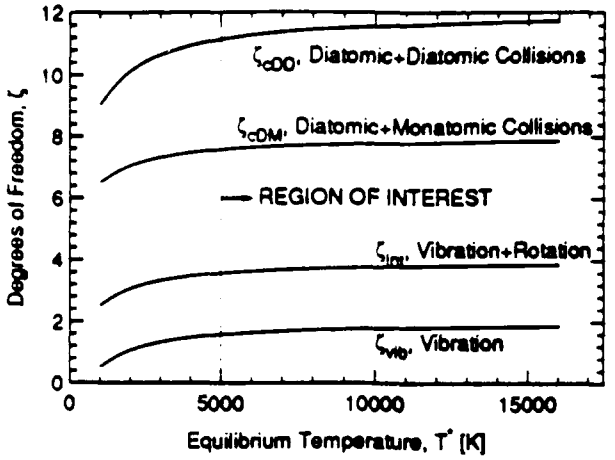


Fig. 2. Temperature variation of degrees of freedom in vibration ($\zeta_{vib}$), internal modes ($\zeta_{int}$), diatomic-monatomic collsions ($\zeta_{c_{DM}}$), and diatomic-diatomic collisions ($\zeta_{c_{DD}}$) when $\theta_{vib} = 2,270K$.

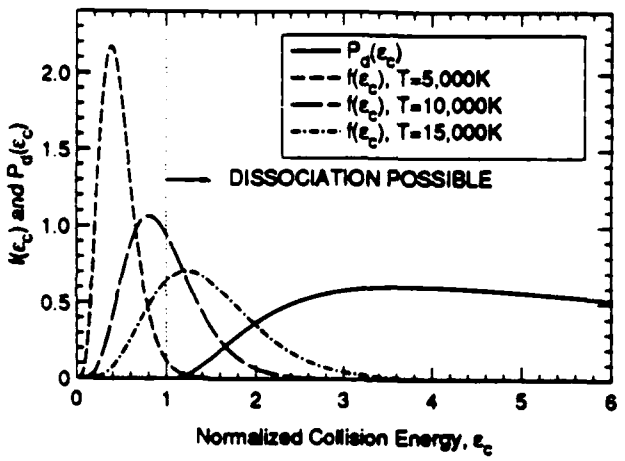


Fig. 3. Reaction probability function, $P_d(\epsilon_c)$, and collision energy distributions, $f_c(\epsilon_c)$, where $\epsilon_c = \epsilon_c/E_d$, for dissociation via $O_2 + O_2$ collisions at $5,000K$, $10,000K$, and $15,000K$.

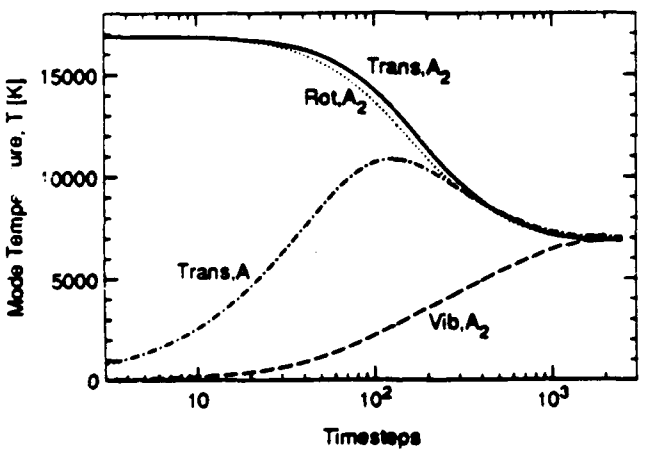


Fig. 4. Temperature per mode per species in $A_2$ thermochemical relaxation from $16,871K$ to $7,000K$.

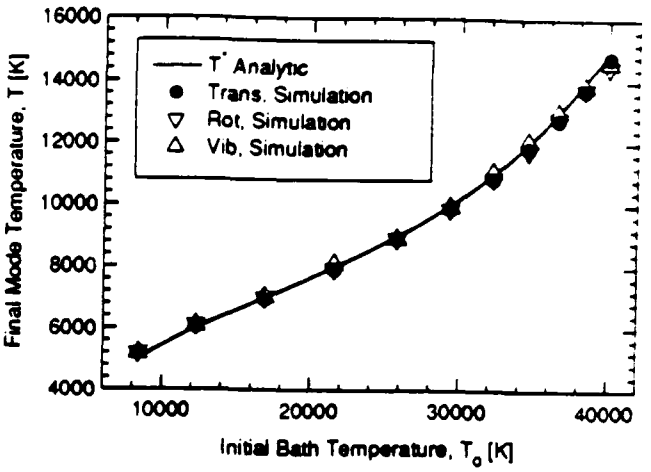


Fig. 5. Simulated vs. analytic equilibrium temperature per energy mode, $T^*$ in $A_2$ relaxation.

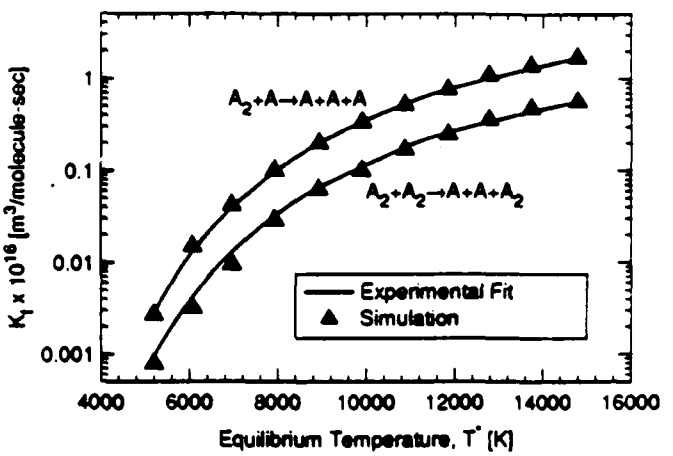


Fig. 6. Simulated forward rate, $k_f$, vs. equilibrium temperature compared with experimental fit in $A_2$ relaxation.

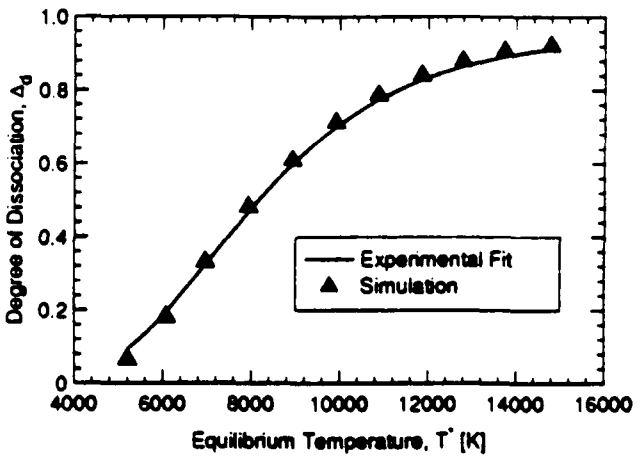


Fig. 7. Simulated degree of dissociation, $\Delta_d$, vs. equilibrium temperature compared with experimental fit in $A_2$ relaxation.

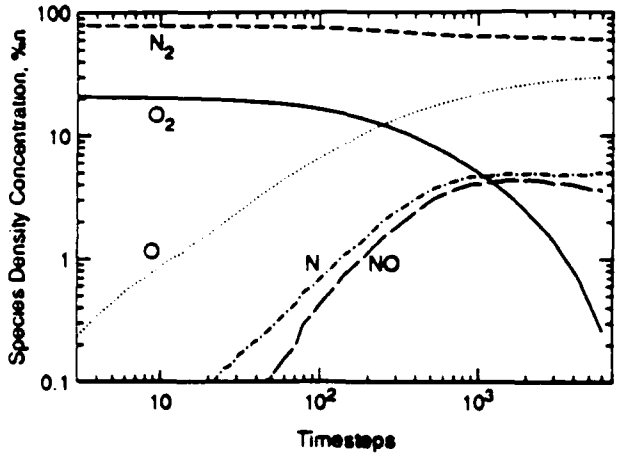


Fig. 8. Percent concentration per species in thermochemical relaxation of air, superheated in translation and rotation at $15000K$.

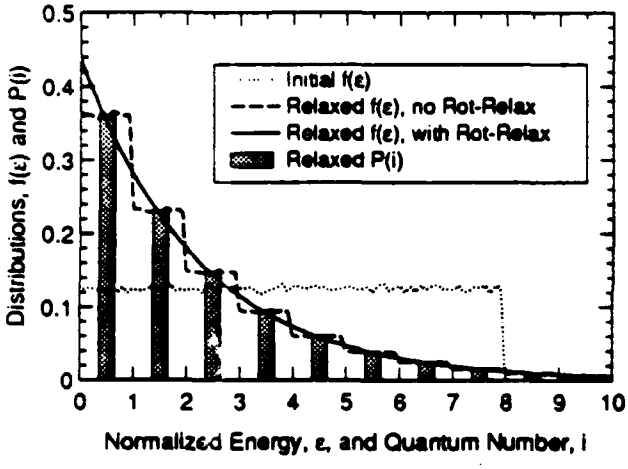


Fig. 9. Relaxation of discrete and continuous energy distributions toward equilibrium at steady-state via mixing algorithm, with and without rotational-relaxation steps.